Development of the Automation Framework and Rebound-Capture System for a Drop-Weight Test Machine

Diogo Rui Ribeiro de Sousa

U. PORTO

FEUP FACULDADE DE ENGENHARIA
UNIVERSIDADE DO PORTO

Mestrado Integrado em Engenharia Mecânica

Supervisor: Prof. António Mendes Lopes

Co-Supervisors: Inv. Carlos Moreira da Silva
Prof. Lucas FM da Silva

June, 2017

Development of the Automation Framework and Rebound-Capture System for a Drop-Weight Test Machine

Diogo Rui Ribeiro de Sousa

Mestrado Integrado em Engenharia Mecânica

June, 2017

Resumo

O estudo de adesivos e juntas adesivas é o foco principal do ADFEUP (Grupo de Adesivos da Faculdade de Engenharia da Universidade do Porto). Uns dos testes mais importantes executados pelo grupo são os testes de impacto, por isso é do seu interesse possuir uma máquina capaz de executar estes testes, nomeadamente, uma *Drop-Weight test machine*, que tem estado no processo de projeto e construção nos últimos anos.

Esta tese continua o trabalho feito por Castro, Barbosa e Ramos, e traz esta máquina um passo mais perto de estar concluída. Isto inclui o projeto, desenvolvimento e implementação de toda a eletrónica da máquina, o desenvolvimento de uma sequência de comando implementada sob a forma de um programa de Simulink® capaz de fazer funcionar a máquina, a implementação e ajuste de um controlador para o motor do sistema de elevação e o projeto e verificação por simulações de um sistema de captura de ressalto a ser instalado no futuro.

ii

Abstract

The study of adhesives and adhesive joints is the main focus of ADFEUP, (Adhesives Group of the Faculty of Engineering of University of Porto). Some of the most important tests performed by this group are impact tests, and so, it is in their interest to have a machine that is capable of performing these same tests, namely a Drop-Weight testing machine, which has been in the process of design and construction in the last few years.

This thesis continues the work done by Castro, Barbosa and Ramos, and aims to bring this machine one step closer to being finished. This includes the design, development and implementation of the electronics of the machine, the development of a command sequence implemented in the form of a Simulink® program capable of running the machine, the implementation and tuning of a controller for the lifting motor and the design and verification through simulation of a rebound-capture system to be installed in the future.

Agradecimentos

Em primeiro lugar, gostava de deixar um agradecimento ao Prof. António Mendes Lopes, ao Inv. Carlos Moreira da Silva e ao Prof. Lucas da Silva, pela orientação e pela incrível disponibilidade que sempre demonstraram ao longo deste trabalho.

Ao grupo de adesivos, ADFEUP, pela ajuda, pela disponibilidade e pela boa disposição que tanto contribuíram para o sucesso desta tese.

Um muito especial agradecimento ao Sr. Joaquim pela enorme ajuda dada no desenvolvimento do sistema elétrico da máquina, pelo tempo disponibilizado, e pela sempre jovial atitude que tanto o carateriza.

Aos grandes amigos Duarte Lacerda, Bárbara Correia, Ulyana Horbatyuk, Joana Machado e Francisco Sousa pela forte amizade e pela infindável paciência.

E finalmente, à minha família pelo forte apoio que demonstraram ao longo de todo o meu progresso académico, e não só.

Diogo Sousa

"Science is the best thing humans beings have ever come up with.
And if it isn't, science will fix it."

Bill Nye

Contents

List of Figures

List of Tables

Chapter 1

Introduction

1.1 Context

In recent years, research into adhesive joints has increased in interest, mainly due to the many advantages that these types of joints bring over traditional mechanical joints. Due to the fact that they work on the basis of adhesive forces, the properties of adhesive joints are significantly different from those based on screws, rivets, welds and others.

Given that the use of these types of joints is still in expansion and development, their mechanical behaviour, in general, is still not as well understood as the behaviour of mechanical joints. This fact, along with the increasing interest in their implementation (especially in the automotive and aero-spacial industries) makes them a very important focus of study. One of the types of adhesive joints that is most used in these applications is the single lap joint (SLJ), due to its simplicity and effectiveness (fig. 1.1). The static behaviour of SLJs is relatively well understood but it's becoming increasingly important to understand their behaviour under impact to guarantee the structural integrity of their application.
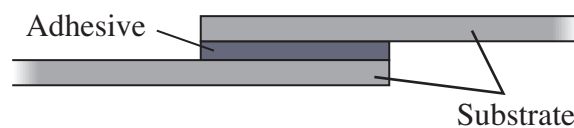
Figure 1.1: Single Lap Joint

1.1.1 Impact Testing

Impact can be defined as a high force being applied over a very short, almost instantaneous period of time, which is usually observed in a collision between two solids. When an adhesive joint is affected by such forces, it is subjected to high strain rates, and it can be desirable to understand it's behaviour under these circumstances (for example, in a car crash). In order to collect data about

adhesives under such stresses, one can use several tests designed for the effect (to be discussed in section 1.2).

The Drop-Weight Impact test, for example, is a type of impact test that is rather simple in concept. It consists in dropping a set weight (equipped with an impactor) under gravity from a controlled height and having it strike a sample joint below. The sample is then carefully studied to learn about the effects of the impact. These tests are usually carried out in machines designed specifically for the purpose, such as the one about which this thesis revolves.

Usually, upon striking the sample, the impactor will end up rebounding (due to the massive weight and high speeds) and if not halted properly, will fall back down and strike the joint a second time, or possibly even more. This can lead to skewed results and is therefore highly unwanted. Thus, it is very important to have a rebound-capture system installed on the machine.

1.2   Literature Review

1.2.1   Adhesives

An adhesive bond is a bond where two components are joined using a layer of adhesive material. The components that are joined together are called the substrates. Due to the fact that adhesives are spread over a large area, the stress concentrations are significantly smaller than in traditional mechanical joints [1], not only because of the very fact that the area of the connection is larger, but also because there is no need to drill any holes in the structure (as in the case of screws and rivets). This corresponds to the whole area of adhesion being under uniform stress, which leads to a better rigidity and better resistance to fatigue effects across the bonded area [1]. This can be seen in fig. 1.2 Adhesives also provide countless other advantages such as better damping across the bonds, reduced weight, cost reduction, and most importantly, the ability to bond different materials such as composites, that could not be bonded otherwise [2].
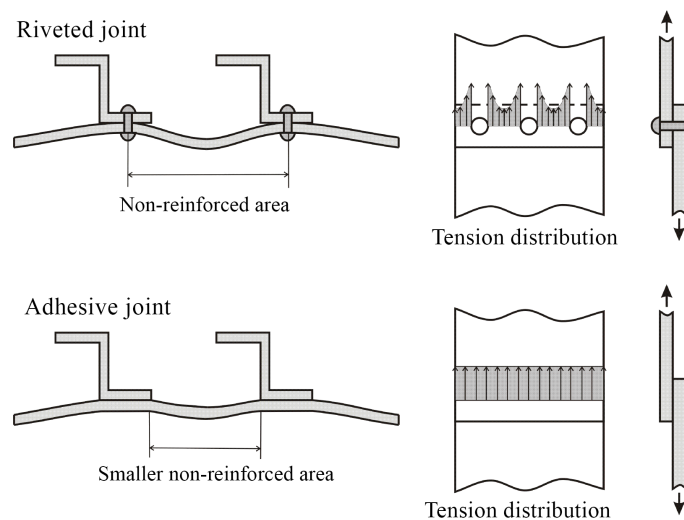
Figure 1.2: A comparison of mechanical and adhesive joints (adapted from [1])

On the other hand, adhesives also possess several disadvantages. The major drawback of using adhesives is their extremely low resistance to forces perpendicular to the plane of the joint, as depicted in fig. 1.3. These forces can lead to tearing of the adhesive layer which ultimately can cause failure of the joint. In fact, it is very important to project adhesively bonded structures in such a way that these forces are reduced to the maximum, which in certain cases can complicate the geometry of said structures. It is always best practice to ensure that the adhesive is under shearing stress. [1]

One difficulty in utilising adhesives can sometimes be the fact that they cannot just be applied as-is, requiring careful surface preparation (be it by mechanical means such as abrasion or chemical treatments) as well as potentially long curing times and conditions (pressure and temperature). Due to its polymeric nature, the chemical stability of certain adhesives can also be compromised by factors such as humidity, heat and UV radiation.
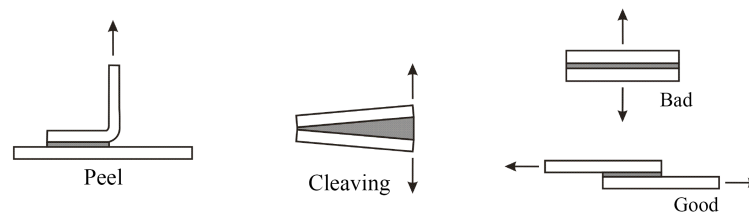
Figure 1.3: Stresses on adhesive joints (adapted from [1])

1.2.2 Impact Tests for Adhesives and Adhesive Joints

As mentioned in section 1.1.1, in order to obtain information about the behaviour of certain adhesives and adhesive joints under impact, there is a myriad of different tests that can be performed. These tests can essentially be divided into two categories: Those used to determine properties of the adhesive materials themselves, and those used to determine the properties of entire adhesive joints [2]. In this subsection, a brief description of these tests is given.

1.2.2.1 Adhesive Material Testing

The properties of most adhesives can vary extensively with strain rate, as briefly mentioned in section 1.1.1. Hence, before moving onto testing adhesive joints, it is very important to understand the behaviour of the adhesive itself in high strain rate (impact) conditions. Some important properties to obtain are [2]:

- Tensile stiffness;

- Shear stiffness;

- Tensile strength;

- Shear strength;

• Fracture toughness (mode I, mode II and mixed mode).

There are many possible tests that can be performed on adhesives. Some, like most tensile tests, are applied on bulk specimens (specimens completely comprised of adhesive material) while others are applied on specimens that do contain a substrate. These latter specimens, however, are designed to minimise any effects caused by the substrate itself. Examples include the thick adherent shear test, the torsion test and the Arcan test [2].

1.2.2.2   Adhesive Joint Testing

In a real world application of adhesives, they are always implemented in some sort of joint. The geometry and structure of said joint, as well as the surface preparation, mechanical proprieties of the substrate and a variety of different factors can influence the final behaviour of the joint, so testing adhesive joints is absolutely imperative to get a good understanding of its proprieties. Examples of tests applied to adhesive joints include the Block Impact Test [3], the Split Hopkins Bar and the Drop-Weight Test, the latter being of great importance for this thesis.

1.2.3   Drop-Weight Test Machines

Models of Drop-Weight Test machines, while they may not be designed specifically for testing adhesives, are currently available on the market. A few examples of commercial machines are presented in this chapter.

1.2.3.1   Instron CEAST 9300 Series

Composed of Models 9310, 9340 and 9350 (Standard and with High-Energy System), the CEAST 9300 series is a set of Drop-Weight Test machines, by Instron (see fig. 1.4). Among them, they can perform impact tests ranging from the low-energy 0.15 J on the CEAST 9310 to the high-energy 1330 J on the CEAST 9350 (with the High-Energy System).

Figure 1.4: From left to right, CEAST 9310, 9340, 9350 and 9350 with High-Energy System (adapted from [4])

The smallest of the set, the 9310, is a tabletop machine (max drop height of 0.7 m) capable of only low-energy testing on small samples (max 20.4 J). The rest of the series is all comprised of large floor-mounted machines, and as the series number increases so does the maximum energy. These machines can be used as-is but a few add-ons are available, such as thermal chambers and rebound-capture systems [4]. A comparison of the series is presented in table 1.1.

Table 1.1: A comparison of CEAST 9300 Series machines [4]

		9310	9340	9350	9350 (with High-Energy System)
Energy (J)	Min	0.15	0.30	0.59	0.59
	Max	20.4	405	757	1800
Height (m)	Min	0.03	0.03	0.03	0.03
	Max	0.70	1.10	1.10	29.4 (simulated)
Mass (kg)	Min	0.5	1.0	2.0	2.0
	Max	3.0	37.5	70.0	70.0

1.2.3.2   Zwick Roell HIT 230F

The HIT 230F, by Zwick Roell, is a Drop-Weight Test machine designed mostly for use with impact tests on plastics and for Compression-After-Impact (CAI) tests on composites (see fig. 1.5a). Much like the machine proposed by Ramos [5] (see section 1.3), this machine has an open structure and therefore allows very easy integration with external apparatuses, such as custom large specimens, temperature control systems, external sensors and various others.

This machine can obtain a variable drop height, ranging from 0.11 m to 1.0 m, which allows for a maximum velocity of 4.4 m/s on impact [6]. If the version of the machine used is prepared for testing plastics, the dropped mass is fixed at 23.5 kg and cannot be changed, but if the CAI test version of the machine is used, the dropped mass is modular and can vary according to the necessary test conditions [7]. With this version, a rebound-capture system is also installed. The same company also possesses some models for high-energy drop weight impact testing that can drop up to 2044 kg from a height of 5 m, which allows for energies up to 100 kJ [8].

1.2.3.3   Imatek IM10 Series

A third company that produces Drop-Weight Test machines is Imatek, with their IM10 series (see fig. 1.5b). This series contains machines for medium to high energy ranges, though with an optional add-on, they can be equipped with low-mass carriages that allow for low energy testing as well.

These machines are very modular, having the possibility of installing a myriad of other different add-ons such as high-velocity impact option (for impact velocities up to 20 m/s), high-speed
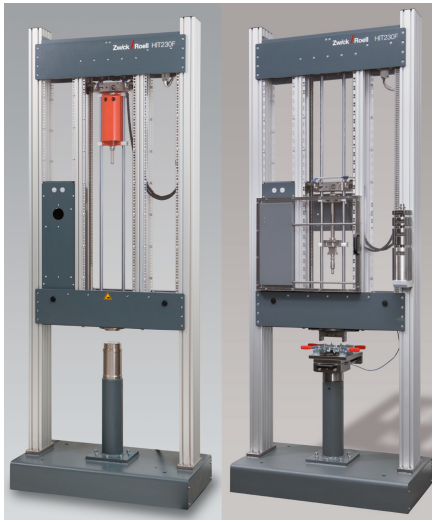
(a) Zwick Roell HIT 230F, for plastics on the left, for composites on the right

(b) Imatek IM10T-20

Figure 1.5: Imatek and Zwick Roell Drop-Weight Test machines

video system to provide visualisation of the test specimen and a thermal chamber. They generally come equipped with a rebound-capture system. Table 1.2 shows a comparison of the different models [9][10].

Table 1.2: A comparison of Imatek IM10 Series machines [9][10]

		IM10R-10	IM10R-15	IM10R-20	IM10T-20	IM10T-25	IM10T-30
Max. Energy (J)		294	440	590	600	750	900
Max. Height (m)		4.0	4.5	5	4.5	5.0	5.5
Velocity (m/s)	Min	1.0	1.0	1.0	1.0	1.0	1.0
	Max	4.43	5.42	6.26	6.26	7.0	7.7
Mass (kg)	Min	-	-	-	5	5	5
	Max	-	-	-	30	30	30

1.2.3.4   Rosand IFW5

The Rosand IFW5 (fig. 1.6) is the machine currently in use by ADFEUP to test adhesive samples. It has a maximum impact energy of 300 J at 4 m/s which is currently not enough to carry out some of the higher energy tests required by the group [5].

Figure 1.6: Rosand IFW5

1.3   ADFEUP Machine

ADFEUP, the adhesives group at FEUP, is dedicated to study and research into Adhesives, Adhesive joints and their applications. Often, inserted in the many research projects, it is necessary to perform impact tests. Currently, FEUP possesses a Drop-Weight Test machine (see section 1.2.3.4) but it is proving too limited for the required tests. As such, there has been work directed into designing and constructing a machine capable of performing Drop-Weight Tests on adhesive samples and joints.

This design has been the main focus of 3 other theses (by Castro [11], Barbosa [12] and Ramos [5]), where the main structure of the machine was designed and constructed (shown in fig. 1.7). The detectors and actuators of the machine were also chosen but had not been implemented, and no circuitry for installing them had been thought out.

In terms of the command sequence, a very general plan had been decided on, consisting in a few routines and how they were going to interact. However, the routines had not been defined properly not had they been implemented in any sort of program.

The original specifications set for the machine were as follows:

- Maximum impact energy: 700 J;

- Minimum impact energy: 50 J (at maximum velocity);

- Maximum velocity on impact: 5 m/s;

- Anvil positioning resolution: 1 mm;
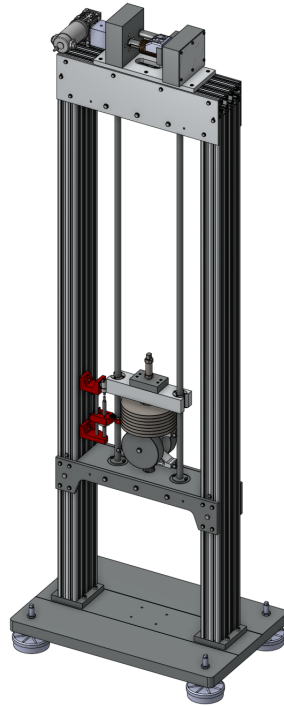
Figure 1.7: Machine structure, as designed by Ramos

1.4   Objectives

It is the main objective of this thesis to complete the framework of a Drop-Weight Test machine. Finalising the framework consists in:

- Projecting a rebound-capture system for the machine;

- Designing and assembling the electrical system of the entire machine;

- The development and implementation of the command software (in MATLAB);

- The development and tuning of a PID position controller to control the lifting motor responsible for positioning the carriage carrying the weight.

1.5   Thesis Layout and Methodology

This thesis is organised into six chapters that cover all the different and relevant aspects of the work done, both in the development of the rebound capture system and in the Drop-Weight Test machine itself.

Chapter 2 details the mechanical design process of the rebound-capture system, ranging from the geometric model of the mechanism to the final CAD design that is to be fabricated and including all the simulations performed to ensure the structural and functional applicability of the system under the working conditions of the machine.

Chapter 3 pertains to both the design of the electronics of the machine, as well as the revision and implementation of the command sequence in Simulink®.

The control system for the main motor is then discussed in Chapter 4.

Finally, Chapter 5 concludes this thesis and provides a proposal for future work to be done on the machine.

Chapter 2

Rebound Capture System

As briefly discussed in section 1.1.1 a rebound-capture system (RCS) is crucial in obtaining accurate and useful data when testing adhesives under impact in a drop-weight test machine. Therefore, one of the first priorities in this thesis was to design one of these systems to be incorporated into the structure assembled by Ramos [5]. The final design of said system is depicted in fig. 2.1. This chapter details the entire process from the initial concept, down to the structural simulations of the final design.
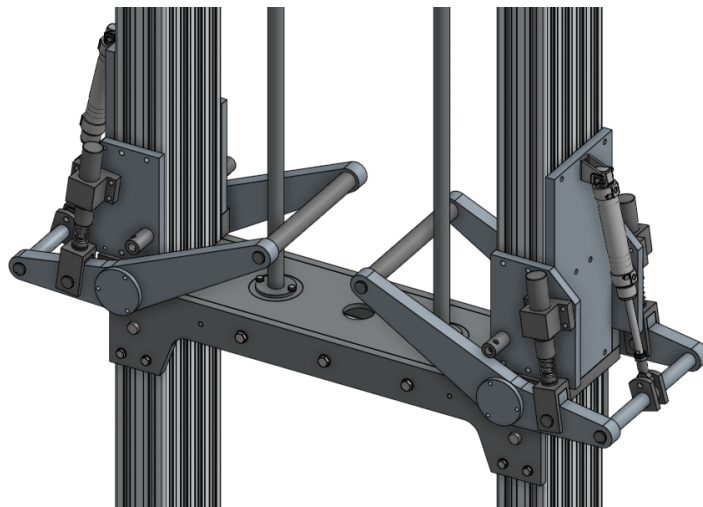
Figure 2.1: Model of final Rebound-Capture System

Before designing the concept, however, it was necessary to define the basic requirements of the RCS. Functionally, it should be able to act not only as a rebound-capture system but also as a safety guard against the possible unwanted release of the anvil. This means that the structure must be able to withstand impact forces equivalent to the worst-case scenario of having the anvil fall from the highest point of elevation, at full mass capacity. Utilizing simulations, Ramos [5] calculated this force to be roughly 33.44 kN. Besides this, the RCS should also be capable of dissipating the impact energy equivalent to this exact situation, 700 J. The system should also be

able to act fast enough to stop any and all rebounds, so an estimated limit of 0.3 s was defined for full actuation time of the system. This is also rather important in an emergency situation, where it is imperative that the RCS act as fast as possible.

Finally, it was also required that, after capture, the anvil should stand 150 mm above the sample, in order to provide enough space to allow handling and removal of the sample.

2.1   Concept and Geometric Model

Upon having the requirements settled, the next step was to decide on the main concept behind the operation of the RCS. Upon studying existing methods implemented in real, commercial machines and considering their advantages and disadvantages, a decision was made to follow a completely different approach to rebound prevention.

(a) Active position   (b) Inactive position
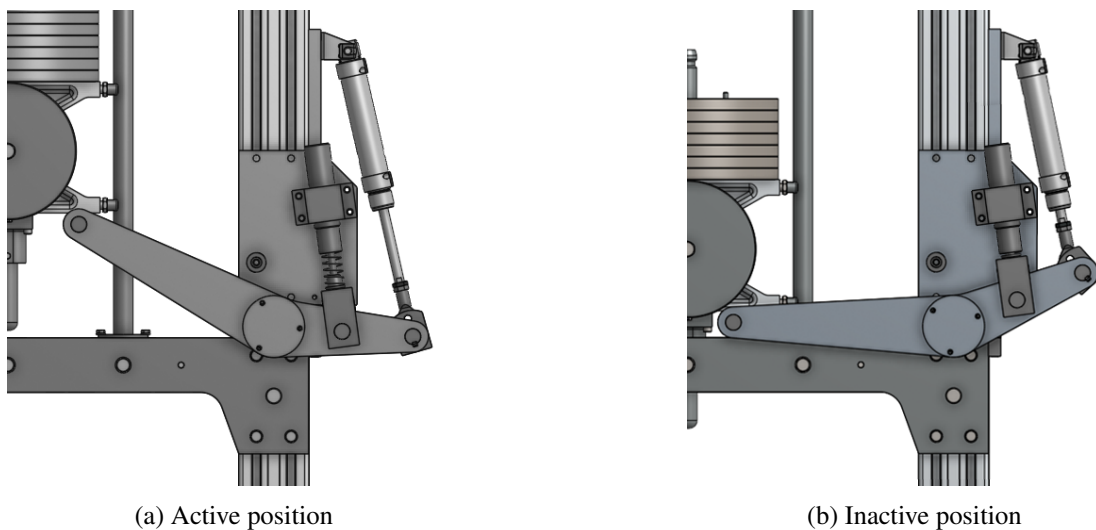
Figure 2.2: RCS in its active and inactive positions

This approach consists of an active system actuated by pneumatic actuators, that works on the principle of a lever. The mechanism, as depicted in fig. 2.2 and fig. 2.3, consists of an arm, usually horizontal when inactive, that when pushed by the fast-acting pneumatic actuators (one per arm), rotates up to meet the falling anvil, preventing it from falling further and striking the sample. Shock-absorbers are implemented in order to absorb the energy on impact.

2.1.1   General Geometry

A simple diagram depicting the dimensions of the proposed system is shown in fig. 2.3. This diagram shows the main arm of the system (points *AOB*) as well as the actuator (points *PA*). While the overall topology of the RCS is well-defined, in order to have a workable geometric model, there are a few dimensions that need to be obtained, namely:

- l and x_{max}, the body length and maximum stroke of the actuator, respectively;
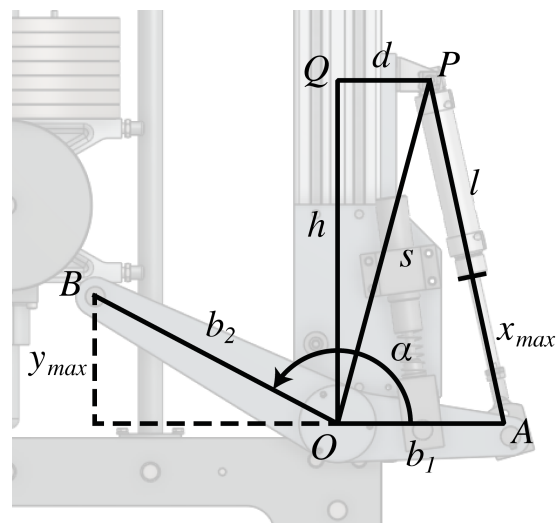
Figure 2.3: Dimensions of the RCS

- b_1 and b_2, the lengths of the sections of the main body;

- α, the angle between both sections of the arm;

- d and h, the horizontal and vertical positions of the pivot point of the actuator.

The approach taken to obtain these values was an iterative one. First of all, b_2 and α were determined, since they are fully dependent on the geometry of the machine. After that, these measurements, along with other factors, were used to select a potential pneumatic actuator, and the system was dimensioned according to this selection. Following this, simulations were run to verify its applicability under working conditions (presented in section 2.3 and section 2.4).
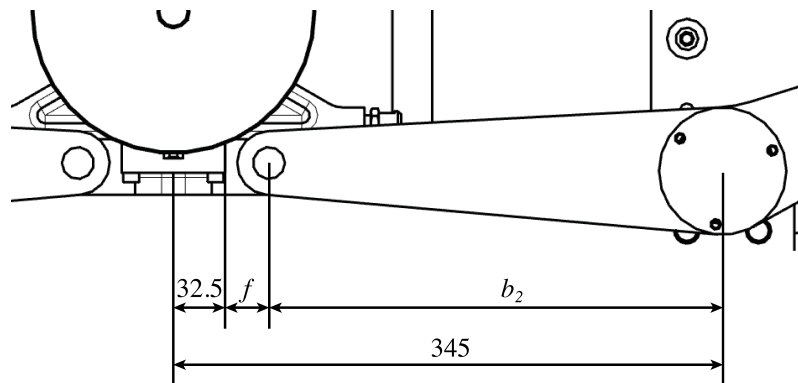
Figure 2.4: Constraints for b_2 (simplified drawing)

Obtaining a value for b_2 was relatively easy when observing the dimensions of the structure of the machine (shown in fig. 2.4). From such figure, we can obtain the following equation:

$$b_2 = 345 - 32.5 - f \tag{2.1}$$

where f is the free space between the impactor and the arm. Choosing a value of 25 mm for f we then obtain that b_2 should be around 287.5 mm, which was then rounded down to obtain a more manageable 285 mm.

From this definition of b_2 and from the diagram in fig. 2.3 it was then possible to define α by the simple trigonometric relation:

$$y_{max} = b_2 \cdot \sin \alpha \tag{2.2}$$

It is possible to equate y_{max} to the distance between the impactor and the sample after the test, which was previously chosen to be 150 mm. From this we obtain an angle $\alpha \approx 148.2°$, which was rounded up to 150°. This rounding up, of course, implies a slightly smaller y_{max} of 142.5 mm, but this 5% difference does not influence the system greatly.

Having determined these initial dimensions, it was then possible to do calculations that helped select a potential pneumatic actuator, starting with the minimum stroke, and following with the minimum diameter. The minimum stroke was selected by approximating it to the vertical displacement of the rear of each arm (line *OA*). This, of course, does not represent the real stroke, since the actuator is tilted in relation to the vertical axis, nevertheless, it is a good initial approximation that can give an idea of the rough magnitude required. Figure 2.5 shows how the rear of the actuator sits in both the active position and the inactive position. From this, we can extract the following relation:

$$\Delta y = b_1 \cdot \sin(180° - \alpha) \tag{2.3}$$

(a) Active position   (b) Inactive position
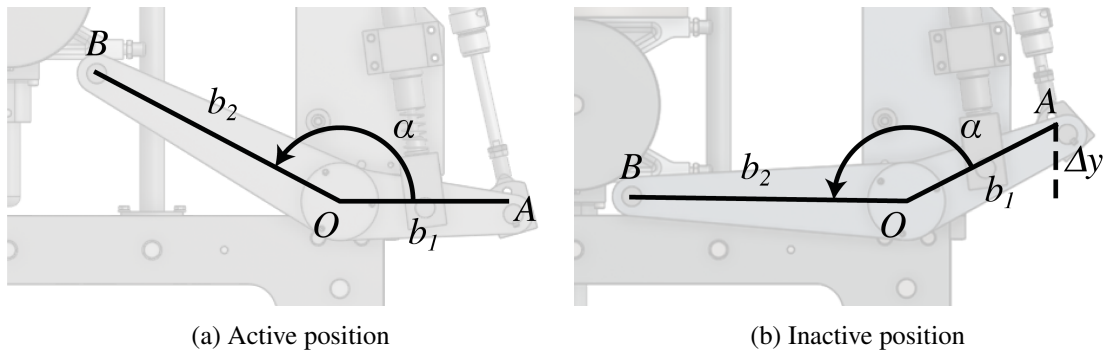
Figure 2.5: Dimensions of the rear of the arm

While an exact value for b_1 is not yet known, it was considered that a good approximation for its value should be two-thirds of the length b_2. With this in mind, equation 2.3 simply becomes:

$$\Delta y \approx \frac{2}{3} \cdot b_2 \cdot \sin(180° - \alpha) \tag{2.4}$$

and thus it is possible to solve for $\Delta y \approx 95$ mm. In order to compensate for the tilt, the stroke x_{max} must necessarily be larger than Δy, and therefore it is possible to define the first restriction for

selecting the actuator as $x_{max} > 95\,\text{mm}$.

The minimum diameter is selected considering the force required to lift the anvil carrying the maximum mass, 56 kg. Since there are two arms acting on the anvil, each will only have to lift the weight of half the maximum mass, or $W = 274.68\,\text{N}$. Therefore, as shown in fig. 2.6, it is possible to write an equation balancing the moments on the arm:

$$W \cdot b_2 = (p \cdot A) \cdot b_1 \cdot \cos(180° - \alpha) \tag{2.5}$$
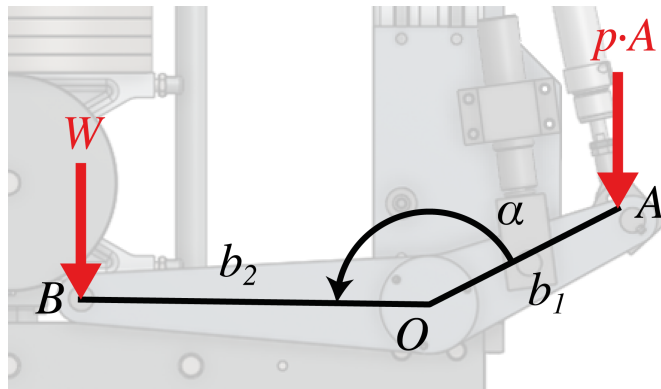
Figure 2.6: Forces on arm when lifting weight

Making the same simplification as for the stroke, $b_1 = \frac{2}{3} \cdot b_2$, it is then possible to calculate the minimum diameter D_{min}:

$$A = \frac{W \cdot \sqrt{3}}{p} \quad \implies \quad D_{min} = \sqrt{\frac{W \cdot \sqrt{3} \cdot 4}{p \cdot \pi}} \quad \implies \quad D_{min} = 31.77\,\text{mm} \tag{2.6}$$

With the restrictions calculated above, the initial choice of pneumatic actuator was selected to be a DSNU-32-100-PPV-A [13] (Figure 2.7), an actuator with a 100 mm stroke and 32 mm diameter and pneumatic damping, along with an MH2 valve [14].
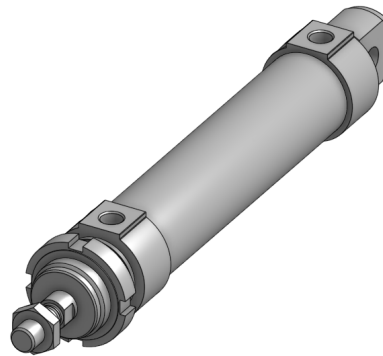
Figure 2.7: Festo DSNU-32-100-PPV-A

In order to install the actuator, some accessories were required, namely:

- Clevis foot mounting LBN-32 [15]

- Rod eye SGS-M10x1.25 [16]

The actuator and the accessories, along with a 16 mm thick aluminium plate (required for mounting on the profiles of the structure), allowed the following dimensions to be obtained:

$$d = 96\,\text{mm} \quad l = 275.5\,\text{mm} \quad x_{max} = 90\,\text{mm} \tag{2.7}$$

The value of x_{max} was reduced from 100 mm to 90 mm in order to prevent shock on the actuator front end, which could damage the pneumatic seal.

(a) Active position   (b) Inactive position
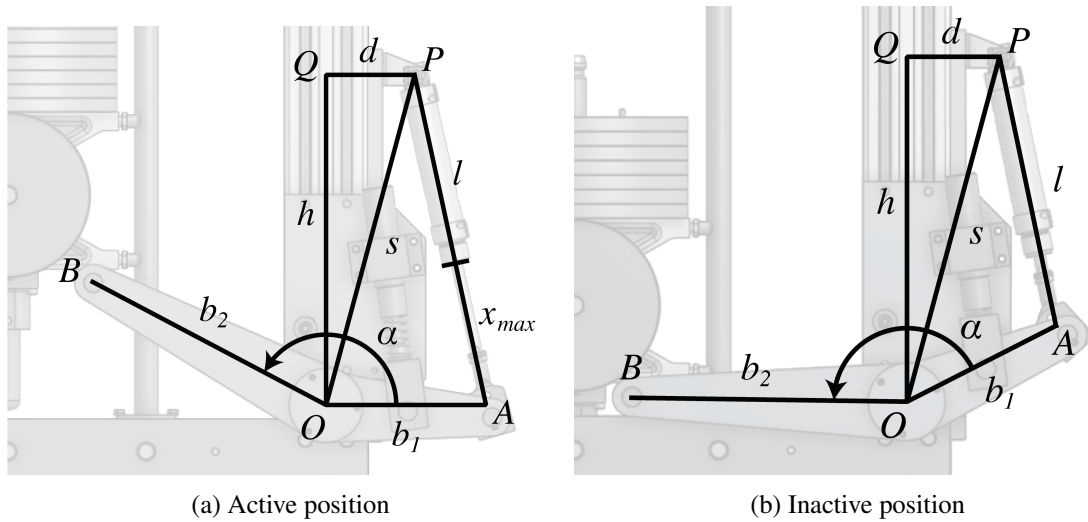
Figure 2.8: Diagram showing relations between dimensions in active and inactive positions

The remaining two dimensions b_1 and h were obtained observing the system in the active and inactive positions (see fig. 2.8). Using trigonometric relations, it is possible to obtain the following two equations:

$$\begin{cases} (d - b_1)^2 + h^2 = (l + x_{max})^2, \\ (d + b_1 \cdot \cos\alpha)^2 + (h - b_1 \cdot \sin\alpha)^2 = l^2 \end{cases} \tag{2.8}$$

which can be solved for b_1 and h to give two possible pairs of results:

$$\text{Solution 1}: \begin{cases} b_1 = 174.1\,\text{mm}, \\ h = 357.1\,\text{mm} \end{cases} \quad \text{Solution 2}: \begin{cases} b_1 = 412.9\,\text{mm}, \\ h = 161.1\,\text{mm} \end{cases} \tag{2.9}$$

Clearly, solution 2 is not very practical. Not only is the arm b_1 far too large, the actuator is also placed very close to the axle (point O). Therefore, solution 1 was selected. To produce more manageable values, they were rounded to:

$$b_1 = 174\,\text{mm} \quad h = 357\,\text{mm} \tag{2.10}$$

2.1.2 Shock Absorption

In order to select the shock absorbers to utilise on the RCS, calculations were made based on the maximum energy required to be dissipated, 700 J (see the beginning of this chapter). Given that each arm will have its own damping system, each arm individually will have to dissipate only half of the total energy, 350 J.

By placing the shock absorbers in a symmetrical arrangement along the frontal plane of the machine, no extra stresses or moments are introduced into the structure of the RCS. This means that either a shock absorber is placed along the middle of the RCS, or a pair of shock absorbers is placed, one at each side. Due to spatial restraints, the latter option was adopted. With each arm having 2 shock absorbers each, the energy dissipation is again distributed, meaning each individual shock absorber only needs to dissipate 175 J.

The energy dissipated along the stroke x of each shock absorber can be expressed by:

$$E = \int_0^x F_d(s)\,ds \tag{2.11}$$

where x represents the stroke and F_d represents the force exerted by the shock absorber. According to ACE, the manufacturer of the model of shock absorber implemented in the final RCS, this force is almost constant along the stroke of the movement [17], as shown in fig. 2.9. While the manufacturer does not provide a scale, it is to be applied on a shock absorber of the same kind as the one used in the RCS (meaning the stroke and force are in the same range), so the small variations in force are not very large.
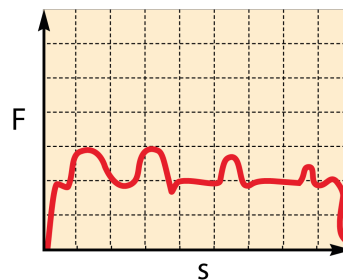
Figure 2.9: Force F as a function of stroke s of an ACE shock absorber (adapted from [17])

By setting $F_d \approx$ constant, equation 2.11 can simplify into:

$$E = F_d \cdot \int_0^x ds \implies E = F_d \cdot x \tag{2.12}$$

Let x_d be the maximum stroke of the shock absorber and $F_{d,max}$ the maximum force it can withstand. Equation 2.11 can then be used to define an inequality that a shock absorber must be able to respect in order to be eligible for implementation:

$$F_{d,max} \leq \frac{E}{x_d} \implies F_{d,max} \leq \frac{175\,\text{J}}{x_d} \tag{2.13}$$

This inequality, along with the condition that the shock absorber can dissipate 175 J of impact energy, is what allows the selection of an adequate model to be implemented.

The model of shock absorber was then selected to be the MC3350EUM-0 from ACE [18] (fig. 2.10). This shock absorber has a stroke of 48.6 mm and an energy dissipation capacity of 310 J per full stroke (well above the required 175 J).
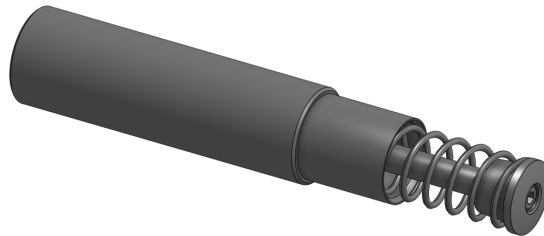
Figure 2.10: Model of a ACE MC3350EUM-0 shock absorber

Ideally, the shock absorber should always act perpendicular to the arm of the RCS in order to reduce the bending moment on its rod and to maximise the force exerted by the shock absorber on the arm. Unfortunately, unlike the arms of the RCS, the shock absorbers are fixed and do not rotate. This means that as the arm rotates up, the angle at which the force from the shock absorber acts will be deviating. A solution to this problem comes in the form of carefully choosing the mounting angle of the shock absorber as to minimise the angle deviation.
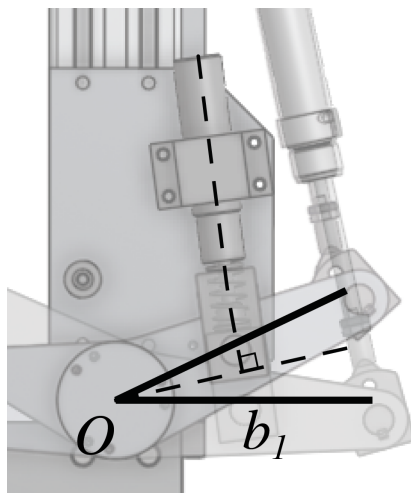
Figure 2.11: Ideal angle for shock absorber

By considering the angle at which the shock absorber must be mounted in order to be perfectly perpendicular to the arm when the latter is at the midpoint of its course (see fig. 2.11), it is possible to minimize the angle deviation to $\pm 15°$, since any other angle would end up reducing this deviation in one direction, but also augmenting it on the other.

With this in mind, the shock absorbers also need to be placed in a position where the arm actuates close to the full stroke length in order to absorb as much energy as possible. For reasons analogous to the pneumatic actuator, it is convenient to not use 100% of the stroke length. Choosing to use only 46 mm, and recurring to fig. 2.12 it is possible to determine the length along the arm that the shock absorber should act on, b_d, which in conjunction with the angle calculated above, pinpoints the ideal position for mounting:

$$x_d^2 = 2 \cdot b_d^2 \cdot (1 - \cos(180° - \alpha)) \tag{2.14}$$
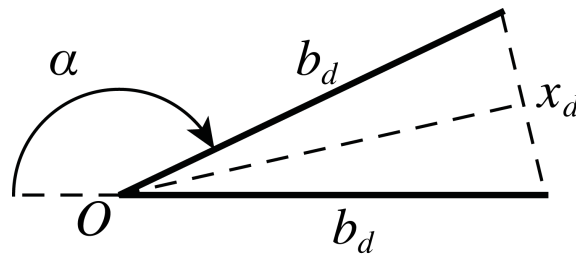
Figure 2.12: Diagram showing the relationship between b_d and the stroke x_d

and from this it was possible to obtain $b_d = 89.9\,\text{mm}$.

2.2 Mechanical Design

The RCS design, as seen previously, is comprised of two identical halves, one on the left side, and one on the right side of the machine. For discussion, each half can be considered to be subdivided into the rotating arm and the fixed structure that attaches to the machine. In this section, an explanation of the construction of these subdivisions is presented in detail.

2.2.1 Arm Construction

The arms, shown in fig. 2.13, are the section of the RCS involved in directly stopping the anvil. In certain situations, they will be the part of the machine that will be under the most stress, so they must be strong enough, while still being rather light to reduce inertia and allow for quick action. The main parts that make up the arms are as follows:

- Main bodies;

- Impact axle;

- Actuation connection;

- Shock absorber pads.
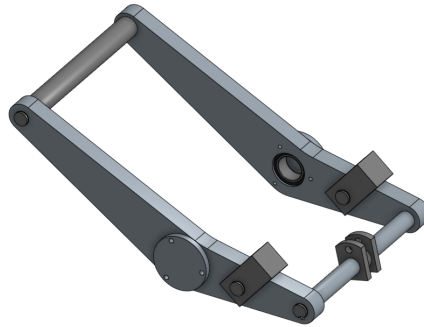
Figure 2.13: Model of one arm of the RCS

2.2.1.1   Main Bodies

The main bodies of the arms comprise most of the moving mass of the RCS, and thus must be
made as light as possible. In order to achieve this without losing mechanical resistance, the arms
are designed to be made out of an aluminium alloy. These are also the parts that will house the
bearings that allow for a smooth and low-friction movement. They had to be carefully dimensioned
to guarantee that they could, in fact, be implemented, and while a calculation of the same nature
was carried out for the shock absorbers, a different approach had to be taken for the bearings.

Figure 2.14: Model of a NA4907-2RSR-XL bearing

The only 3 points of contact between the structure of the RCS and the arms are the shock
absorbers, the pneumatic actuator and the bearings. If a case happens where the shock absorber is
not in contact with the arms (for example if the system is ordered deactivate and activate in a much
too quick succession, the shock absorber may not have time to extend fully), the bearing should be
the point that should be taking most of the load, in order to conserve the actuator. Consequentially,
the bearings should be able to withstand the total shock forces on impact. In a situation such as

this, where the impact forces are so large, it is important to introduce a large safety coefficient. Being a machine designed for tests, the coefficient chosen was 4.0, in order to be sufficiently large to account for potential deviations from the standard stresses on the machine. this means that, with the RCS having 4 bearings in total, each individual bearing should be able to withstand 33.44 kN.

It is desired to have bearings that are as compact as possible, while still being able to handle the high loads imposed by the falling anvil. Due to its simplicity in implementation, ball bearings were considered, but they revealed too bulky to be utilised properly. Needle bearings, on the other hand, offer a high static load rating (radial), in a very compact volume, so they are ideal for this application. With this in mind, the bearing chosen for this application was the NA4907-2RSR-XL [19] (shown in fig. 2.14). It's properties are presented in table 2.1.

Table 2.1: Mechanical characteristics of an NA4907-2RSR-XL bearing

m (g) Mass	C_r (N) Dynamic load rating, radial	C_{0r} (N) Static load rating, radial	C_{ur} (N) Fatigue limit load, radial
175	29500	39500	7200

One major disadvantage of using needle bearings is the fact that they offer very little axial reaction. A consequence of this is that if the construction strategy used does not provide this reaction, the bearing could dismantle at the minimum axial force. In order to provide this force, without having both bodies contact (which would introduce friction into the system and turn the bearing useless) a solution involving a low-friction washer was implemented.

(a) Constructive solution for bearing installation

(b) Reaction forces on bearing outer race
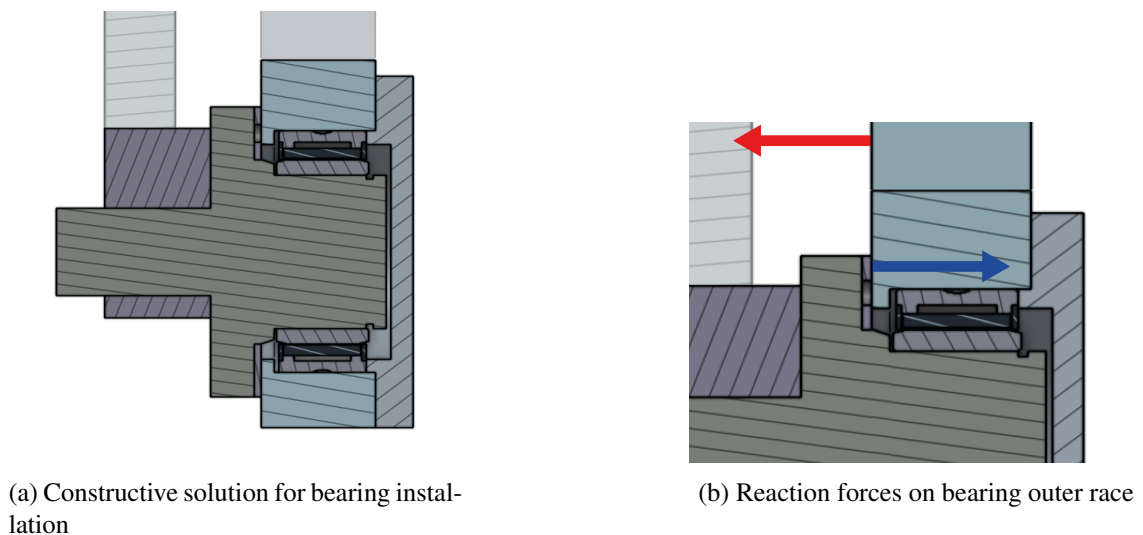
Figure 2.15: Bearing installation

The inner race of the bearing is secured to the axle (which connects to the structure) using a retaining ring. The outer race is secured in between the arm of the RCS and a lid. Between both, lies a washer, specifically, a EGW42-E40-B [20], a maintenance-free thrust washer with bronze backing to guarantee low-friction contact. This washer prevents the bearing from sliding to the left

(see fig. 2.15b) while the connection between the arms prevents sliding in the opposite direction. With this constructive method, the bearing is secured in place and axial loads are no longer an issue.

2.2.1.2 Actuator Connection

The actuator, in order to move the RCS's arms, needs to act on an axle. Unfortunately, the rod eyes available from Festo for the chosen pneumatic actuator do not have diameters that are appropriate for this use, because they are far too small. On an axle with over 300 mm in length, having a section with 10 mm is not enough to handle the forces imposed by the actuator, since it would create a far too large bending moment which would lead to failure of the axle.

(a) Model of the connecting part

(b) Actuator fully extended, showing alignment of axles
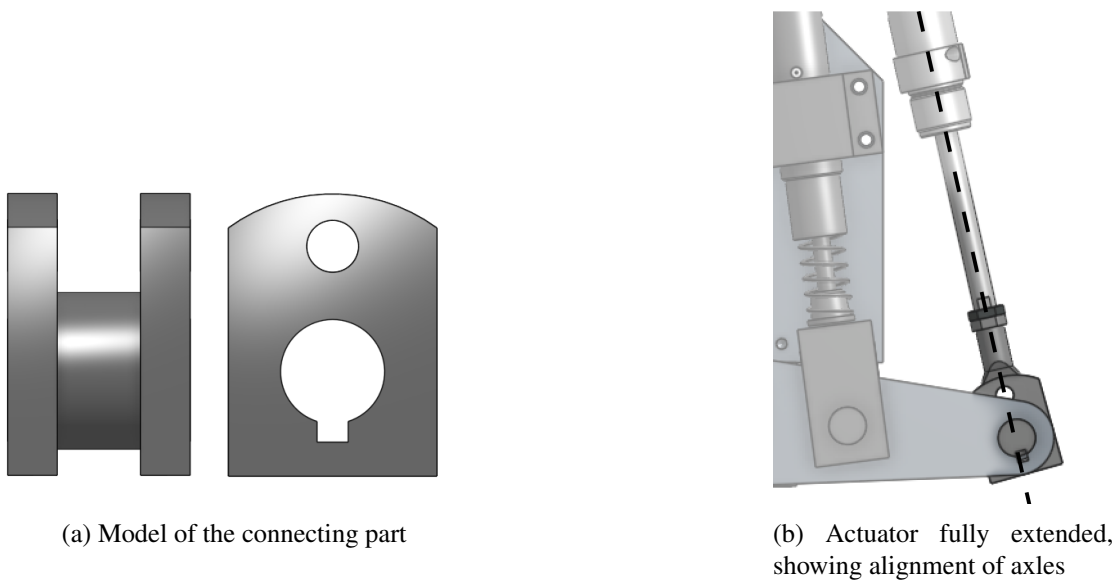
Figure 2.16: Diagram showing relations between dimensions in active and inactive positions

Instead, in order to allow for a larger diameter, a specially designed connection part is used. It consists of a steel piece with two bores, one for a small 10 mm axle for connection with the actuator itself, and one for a larger axle that connects to the arm. In order to prevent rotation of this part, the axles are locked in place using keys. Furthermore, the connecting part is positioned in such a way that when the actuator is fully extended, the part is perfectly aligned with the rod, leading to better transmission of force without introducing torsion stresses on the larger axle (see fig. 2.16b).

2.2.1.3 Shock Absorber Pads

The point where the shock absorbers contact the arms of the RCS will be a point where a lot of stress will be built up. Therefore, it is very important that the force acts perpendicularly to the arm, to avoid stress concentrations and dents. For this reason, special pads were designed to guarantee permanent perpendicularity of the shock absorbers as shown in fig. 2.17.
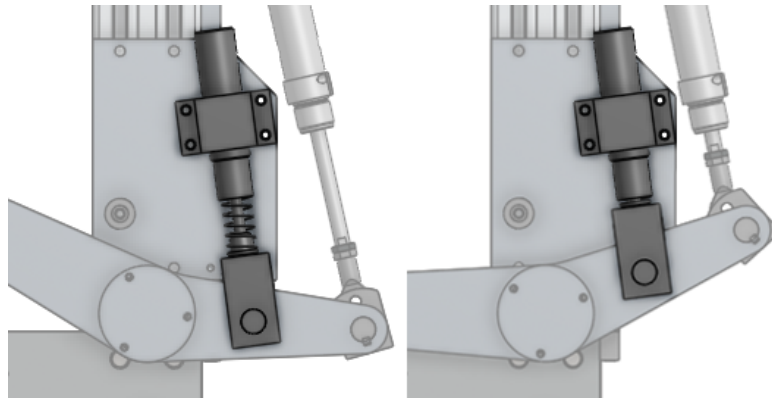
Figure 2.17: The shock absorber always acts perpendicular to the arm

These pads rotate around axles locked by retaining rings on both sides of each arm. Given this free rotation, it could happen that in the situation where the system activates, if the shock absorbers don't extend fast enough, the pads could rotate out of the way, as shown in fig. 2.18a.
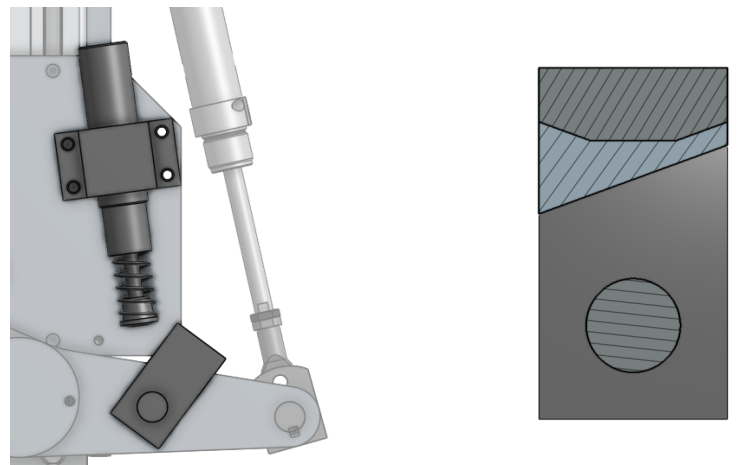
(a) Without some way to maintain alignment, the pads can easily rotate out of the way of the shock absorbers

(b) Halfway cut of the alignment pad, showing the polyurethane block in blue

Figure 2.18: Diagram showing relations between dimensions in active and inactive positions

In order to fix this, the pads need to have a system in place to guarantee alignment. The solution adapted for this application was a block of polyurethane under the pad (fig. 2.18b). This material is rather resilient, being used often in components for hydraulic press bending machines. This block keeps the pad pointed at the shock absorber when it is not in contact, and when the shock absorber contacts the pad, it can easily compress to allow for the required rotation of the pad.

2.2.2 RCS Structure Construction

The structure, shown in fig. 2.19, is the part of the RCS that performs the link between the active components of the RCS (arms, actuator and shock absorbers) to the main structure of the machine. It is essentially constructed with 16 mm aluminium plating along with some steel parts where the stresses are largest in the structure. It also contains the axles where the arms ride on, attached to the structure through 2 steel blocks, and through a bore drilled directly on the vertical aluminium profiles of the structure.
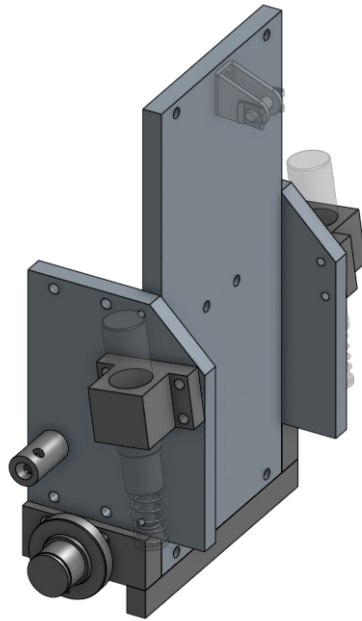
Figure 2.19: Model of RCS Structure

There are three aluminium plates: two plates on the front and back of the machine for housing the shock absorbers, and one on the side for housing the clevis foot mounting of the pneumatic actuator. On each of the front and back plates is bolted the holder for the shock absorbers and a small actuator where a screw can be installed, designed to prevent the arm from rotating over a certain angle chosen by the user.

The plates are secured on the profiles of the structure utilising T-Head bolts. While these bolts hold the plates securely against the profile, they shouldn't be put in vertical stress (such as the reaction from the pneumatic actuator extending), since they are likely to slip. Therefore, care was taken to guarantee that all vertical forces were directly or indirectly discharged on the structure of the machine not through the bolts. This is achieved by having the front and back plates connect to the side plate utilising a pin and the latter plate discharge on the axles through a steel bar and two steel blocks.

2.3   Functional Simulations

With the model of the RCS complete, it was possible to run simulations to verify that the system could indeed be actuated in the time required, 0.3 s, as mentioned in the beginning of this chapter. To achieve this, the system had to be mathematically modelled in Simulink® (see fig. 2.20). The model was comprised of the following sub-models:

- Pneumatic valve;

- Pneumatic actuator chamber;

- RCS mechanics;

- LuGre Friction model.

Figure 2.20: Global mathematical model of the RCS

2.3.1   Pneumatic Valve

The movement of the system begins when a signal is given to the pneumatic valve, and air is allowed to flow into the chamber of the actuator. This means that the mathematical model must be able to determine the mass flow of air leaving the valve as a response to a step input given to the solenoid.

When modelling a pneumatic valve, especially when it is a fast-acting valve such as the one used in this system, it is important to consider the compressibility effects of air, and to take into account whether the air moving through the valve ever enters in choked flow. For this reason, the mathematical model for the pneumatic valve is based around the ISO 6358 Standard [21]. According to the standard, the mass flow exiting the valve is given by the following equation:

$$
\dot{m} = \begin{cases} C \cdot p_1 \cdot \rho_0 \cdot \sqrt{\frac{T_0}{T_1}}, & r_p \le b, \\ C \cdot p_1 \cdot \rho_0 \cdot \sqrt{\frac{T_0}{T_1}} \cdot \sqrt{1 - \left(\frac{r_p - b}{1 - b}\right)^2}, & r_p > b. \end{cases} \tag{2.15}
$$

Where:

- $\dot{m}$ is the mass flow;

- C is the sonic conductance;

- ρ is the density of air at room temperature and pressure;

- p is pressure;

- T is temperature;

- r_p is the pressure ratio between the entry and exit of the valve, $\frac{p_2}{p_1}$;

- b is the critical pressure ratio (pressure ratio below which the fluid becomes choked).

And the subscripts 0,1 and 2 represent the conditions of the environment, of the air entering the valve, and of the air exiting the valve, respectively. This graph for this equation is displayed in fig. 2.21.
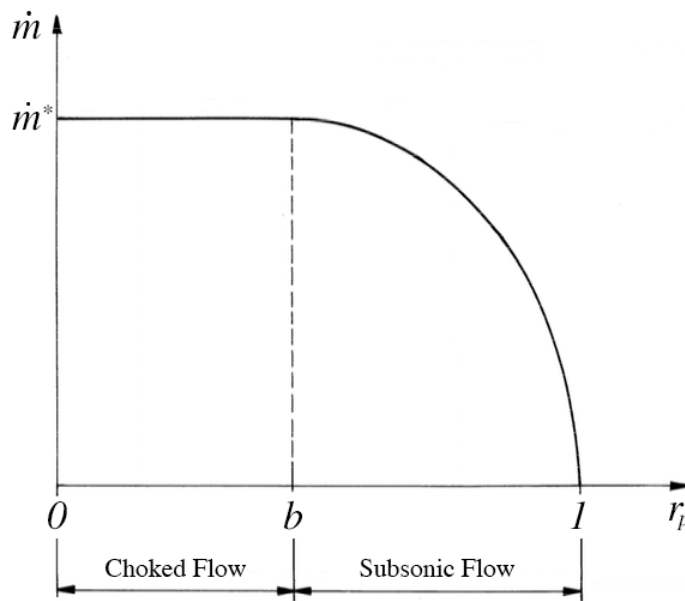
Figure 2.21: $\dot{m}$ as a function of r_p (adapted from [21])

The reason for the discontinuity is due to the fact that when r_p lowers below a certain point, b, the velocity of the air exiting the valve increases too much it becomes supersonic and enters in choked flow. From this point onwards, the mass flow reaches a critical value $\dot{m}^*$ from which it doesn't increase anymore. On the other hand, if $r_p > b$, the fluid is considered in subsonic conditions, and the mass flow will, therefore, depend on the value of r_p. The general shape of the graph of mass flow versus pressure ratio is given in fig. 2.21.

The sonic conductance C of the valve is not divulged by the manufacturer. Hence, an estimated value of $0.02\,(\text{kPa}\cdot\text{s})^{-1}$ is used due to it being a typical value. The value of b for air can be obtained from the following equation [22]:

$$b = \left(\frac{2}{\gamma+1}\right)^{\frac{\gamma}{\gamma-1}} = 0.5283 \tag{2.16}$$

where $\gamma = 1.4$ is the heat capacity ratio of air. In addition to the behaviour above, the mathematical model of the valve also takes into account its commutation time, by multiplying the output of the block ($\dot{m}$) by a unit ramp that takes $2\,\mu\text{s}$ to reach 1 (this value of time is given by the manufacturer of the valve). Due to the fact that the valve has a limit on how much mass flow it can provide, the model also saturates this value to prevent inconsistent results. Figure 2.22 shows the Simulink® block diagram implemented, not including the valve's commutation time.
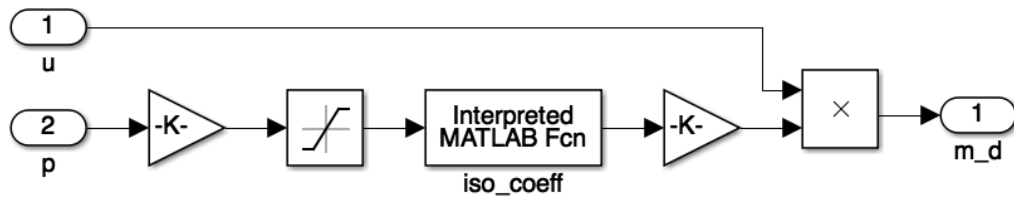
Figure 2.22: Simulink® block diagram for the valve sub-model (not including the valve commutation time dynamics)

2.3.2 Pneumatic Actuator Chamber

The air, once it leaves the valve, heads into the chamber of the actuator. This sub-model is responsible for the thermodynamic behaviour of the air inside the chamber of the actuator as the RCS is actuated. There are many possible implementable models that describe these dynamics; the one chosen is given by the following pair of differential equations [23]:

$$\begin{cases} \frac{dp}{dt} = -\gamma \cdot \frac{p}{V} \cdot \frac{dV}{dt} + \gamma \cdot \frac{R}{V} \cdot \dot{m}_{in} \cdot T_1 - \gamma \cdot \frac{R}{V}\dot{m}_{out} \cdot T - \frac{\gamma-1}{V} \cdot \dot{Q}, \\ \frac{dT}{dt} = \frac{T}{V} \cdot \frac{dT}{dt} \cdot (1-\gamma) - \dot{m}_{out} \cdot \frac{R \cdot T^2}{V \cdot p} \cdot (\gamma-1) + \dot{m}_{in} \cdot \frac{R \cdot T}{V \cdot p} \cdot (\gamma \cdot T_1 - T) - \frac{\gamma-1}{p \cdot V} \cdot \dot{Q} \end{cases} \tag{2.17}$$

where:

- p is the air pressure inside the chamber;

- V is the volume of the chamber;

- $\dot{m}_{in}$ and $\dot{m}_{out}$ are the mass flow in and out of the chamber, respectively;

- T_1 is the temperature of the air entering the chamber;

- T is the temperature of the air inside the chamber;

- $\dot{Q}$ is the heat transfer between the air inside the actuator and its walls;

- R is the specific gas constant of air.

This model, being general for pneumatic actuator chambers, needs to be able to be applied in many different situations. For the application required in this thesis, there are simplifications that can be done that do not compromise its accuracy.

First of all, the model can be applied in a case where it is necessary to actuate a pneumatic actuator both in the forward and reverse directions, hence the existence of both an $\dot{m}_{in}$ and an $\dot{m}_{out}$ term. Since in this case, the only interest is to understand the behaviour of the actuator in the forwards direction, for actuating the arm, the term $\dot{m}_{out}$ can be removed from the equations, leaving only $\dot{m}_{in}$, which equals the mass flow coming from the valve, $\dot{m}$. This leads to the following model:

$$\begin{cases} \frac{dp}{dt} = -\gamma \cdot \frac{p}{V} \cdot \frac{dV}{dt} + \gamma \cdot \frac{R}{V} \cdot \dot{m} \cdot T_1 - \frac{\gamma-1}{V} \cdot \dot{Q}, \\ \frac{dT}{dt} = \frac{T}{V} \cdot \frac{dT}{dt} \cdot (1-\gamma) + \dot{m} \cdot \frac{R \cdot T}{V \cdot p} \cdot (\gamma \cdot T_1 - T) - \frac{\gamma-1}{p \cdot V} \cdot \dot{Q} \end{cases} \tag{2.18}$$

The second possible simplification that can be done to the model comes from the fact that the actuator needs to act in a very reduced amount of time and therefore, it will not have much time to exchange heat to the surrounding area. With this in mind, it is adequate to ignore the terms containing $\dot{Q}$ since they will have very little effect on the model. Once both these simplifications are applied, $\frac{dp}{dt}$ ceases to be dependent on T, and therefore the second differential equation can be dismissed. Hence, the model can be simplified to:

$$\frac{dp}{dt} = -\gamma \cdot \frac{p}{V} \cdot \frac{dV}{dt} + \gamma \cdot \frac{R}{V} \cdot \dot{m} \cdot T_1 \tag{2.19}$$

With this equation, it is possible to simulate the thermodynamic behaviour of air inside the actuator chamber. To actually implement it, however, the following variable substitutions are required:

$$V = A \cdot x + V_0 \quad \dot{V} = A \cdot \dot{x} \tag{2.20}$$

Here, A represents the section of the actuator, x and $\dot{x}$ represent the stroke and velocity of the rod of the actuator, respectively, and V_0 represents the dead volume of the chamber (the volume left over when the actuator is fully retracted, including the volume of the pneumatic tubing). By applying this transformation and some mathematical manipulations, the model of the chamber implemented in the simulations works out to:

$$\frac{dp}{dt} = \frac{\gamma}{A \cdot x + V_0} \cdot (\dot{m} \cdot R \cdot T_1 - p \cdot A \cdot \dot{x}) \tag{2.21}$$

Figure 2.23 shows the actuator chamber sub-model in Simulink® block form.
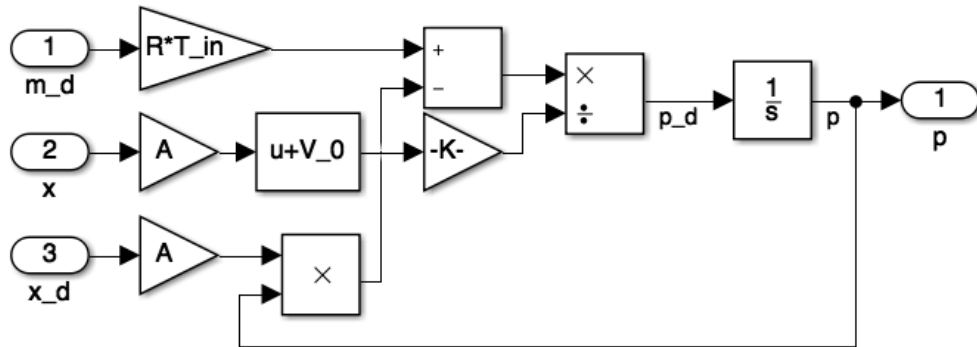
Figure 2.23: Simulink® block diagram for the actuator chamber sub-model

2.3.3 RCS Mechanics

Ignoring friction (further discussed in the next subsection), upon obtaining the pressure inside the actuator, it is possible to calculate the force acting on the actuator rod by simply subtracting atmospheric pressure present in the other chamber of the actuator and multiplying by the area of the piston.

$$F = (p - p_0) \cdot A \tag{2.22}$$

This force, applied by the actuator will move the arm of the RCS, which has an associated inertia. This inertia is an equivalent mass m_{eq} resulting from the inertia associated with the mass of the rod of the actuator, m_{rod}, together with the inertia associated with the rotation of the arm around its axle, J. These values can be obtained from the CAD software. Thus, the value for m_{eq} can be given by:

$$m_{eq} = m_{rod} + \frac{J}{b_1^2} \tag{2.23}$$

Newton's second law can then be applied to obtain:

$$F = m_{eq} \cdot \ddot{x} \tag{2.24}$$

In this model, the effects pertaining to the rigidity of the mechanical components is ignored, since it is negligible when compared to the compressibility of the air and its dynamics, modelled in section 2.3.2. Viscous damping is also ignored because it is taken care of by the LuGre friction model, discussed in the next subsection. Figure 2.24 shows the Simulink® block model pertaining to this sub-model.

This sub-model also takes into account the fact that the actuator has a limited stroke, and it prevents x from increasing indefinitely, and setting $\dot{x}$ and $\ddot{x}$ to 0 once the limit is reached. This, of course, does not include rebound or shock effects, but those are not relevant for this simulation.
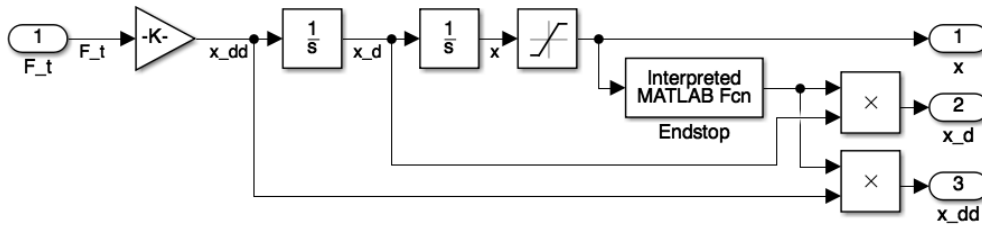
Figure 2.24: Simulink® block diagram for the RCS mechanics sub-model

2.3.4 LuGre Friction Model

Friction plays an important part in this simulation since it opposes the movement of the arm and can end up slowing the actuation by a few fractions of a second. These fractions, in such a short time-scale as is the one in this simulation, can end up making quite a difference, so it is crucial to consider friction as part of the model.

There are essentially 3 sources of friction in the mechanism: the axle of the arm, the axle of the clevis foot of the actuator and the friction of the actuator itself as it extends. However, the first two are so small when compared to the third that they can be safely ignored. To simulate the friction of the actuator, one could use many models ranging from the very simple such as the typical Coulomb friction (with or without consideration of the Stribeck effect) to the more complex Dahl and LuGre models. The latter of these was chosen for this simulation.

(a) LuGre bristle analog

(b) Average bristle deflection
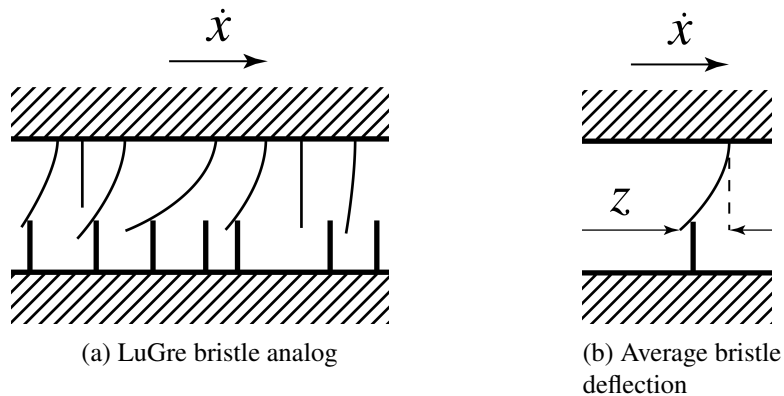
Figure 2.25: LuGre bristle model

The LuGre model mathematically describes the friction force by describing the interaction between two contacting surfaces as deflecting bristles [24] as shown in fig. 2.25a. The average deflection of the bristles is denoted by z and is modelled by equation 2.25.

$$\frac{dz}{dt} = \dot{x} - \sigma_0 \cdot \frac{|\dot{x}|}{g(\dot{x})} \cdot z = \dot{x} - h(\dot{x}) \cdot z \qquad (2.25)$$

Where σ_0 is a constant that represents rigidity of the bristle and $g(\dot{x})$ is a function carefully chosen to impart the behaviour of Coulomb and Stribeck effects in the model (shown in figure fig. 2.26). These effects include:

- Stiction force (F_s), the force of friction at $\dot{x} = 0$;

- Decreasing friction for low $\dot{x}$ down to a minimum friction force F_c, the Coulomb force (Stribeck regime);

- Friction force increasing with crescent $\dot{x}$ from then on, corresponding to viscous friction (viscous regime).
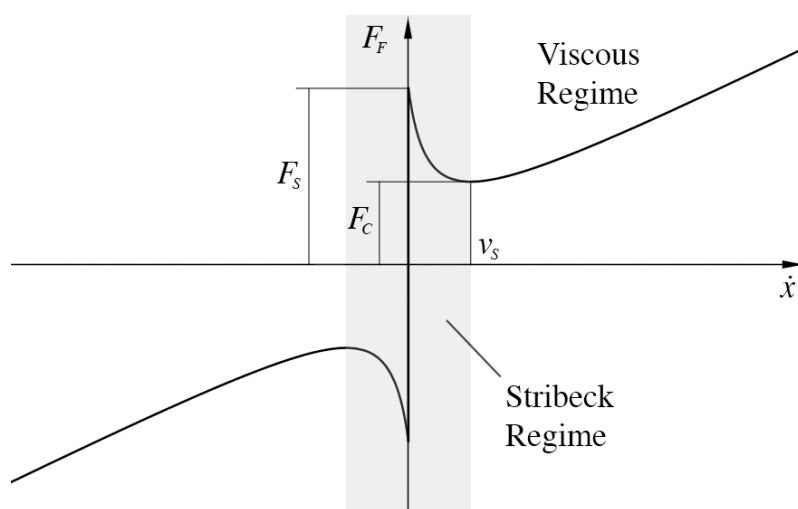
Figure 2.26: LuGre Friction behaviour, showing stiction and Coulomb forces, as well as Stribeck and viscous friction regimes

The first term of equation 2.25 imparts a deflection proportional to the integral of the velocity, and the second term guarantees that the magnitude of the deflection z converges to $g(\dot{x})$ on a steady-state regime [24]. One definition for $g(\dot{x})$, most used in the literature, is the following [25]:

$$g(\dot{x}) = F_c + (F_s - F_c) \cdot e^{-|\dot{x}/v_s|^\alpha} \tag{2.26}$$

where F_C and F_S represent the Coulomb and stiction forces, respectively, v_s represents the Stribeck velocity (velocity for which friction is minimal) and α is a parameter, that can vary between 0.5 and 2 [25].

The average deflection z is then used to calculate the final friction force F_F as:

$$F_F = \sigma_0 \cdot z + \sigma_1 \cdot \dot{z} + \sigma_2 \cdot \dot{x} \tag{2.27}$$

where σ_1 is the damping coefficient of the bristles and σ_2 the damping coefficient of the macroscopic system.

The various coefficients of the model are empirical and thus are usually determined experimentally. For this thesis, typical values for these coefficients for pneumatic actuators were used [26][27], as shown in table 2.2. With these values, the final Simulink® sub-model was designed and implemented as shown in fig. 2.27.

Table 2.2: LuGre coefficients

σ_0	σ_1	σ_2	F_C	F_S	v_s	α
10^5	$\sqrt{10^5}$	100	12	30	10^{-3}	2
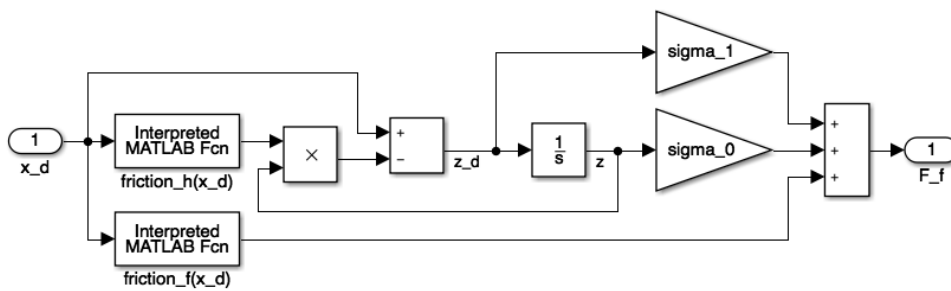
Figure 2.27: Simulink® block diagram for the RCS friction sub-model

2.3.5 Simulation Results

With the complete model, the simulation was run. A few parameters were monitored, namely actuator pressure, the mass flow of air used, acceleration, velocity and most importantly, stroke. The latter is shown in fig. 2.28.
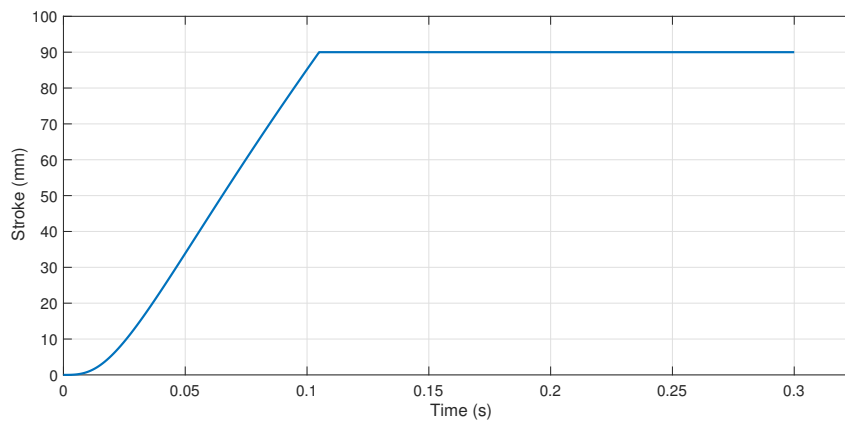
Figure 2.28: Stroke x as a function of time

With these results, it is possible to observe that the actuator is capable of extending its full stroke in less than half of the maximum allowable time. However, it is still necessary to check if the behaviour of the simulation is correct and if the pressure inside the chamber of the simulated actuator is compatible with the real unit.

The pressure of the chamber, as shown in fig. 2.29, behaves exactly as expected. First, there is an increase in pressure at the start of the movement as the air compresses inside the chamber but is not allowed to expand due to the inertia of the system preventing the piston from advancing. As the masses accelerate, the volume of the chamber begins to increase and the air expands, and thus the pressure reduces. This can be seen by the 5 bar peak. Finally, upon reaching the end of the stroke, volume stops increasing, and so the pressure inside the actuator chamber can equalise with the pressure from the air supply. Thus, the maximum pressure inside the actuator chamber is the pressure of the air supply, as expected. Hence, since this value is clearly under the maximum pressure of the actuator, the system, as it is, meets all the planned functional requirements of the RCS.
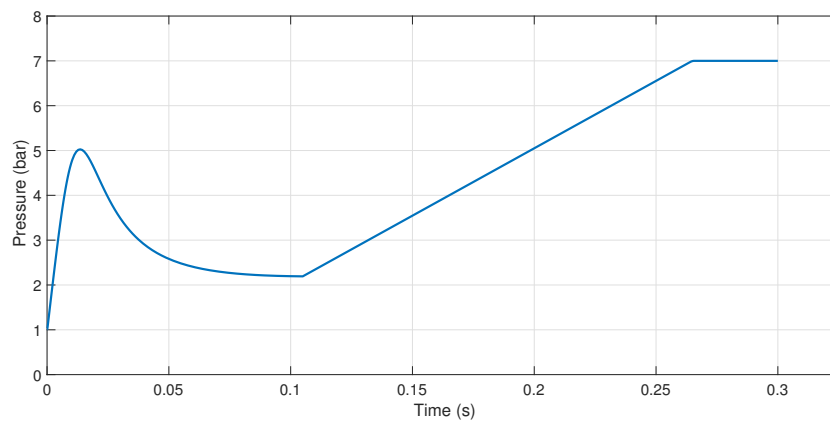
Figure 2.29: Chamber pressure p as a function of time

2.4   Structural Simulations

The last in step in validating the RCS for application was to run a model of the RCS through static studies in SOLIDWORKS to verify the integrity of the structure when under load. These studies concentrated on the most important parts of the structure and omitted any part of the structure that is not essential for the structural resistance and replaced all normalised components with simulated connections. Due to limitations in the software, it was impossible to implement a simulation of the shock absorbers, so these were replaced with rigid connections. Figure 2.30 shows an example of one of these simulations.

The full force of impact is very high at the moment of contact but only happens during a very short time-frame. Hence, it would not be realistic to run simulations using the value of 33.44 kN

calculated by Ramos [5]. Instead, the value 3800 N is used, as calculated for the shock absorbers in section 2.1.2.
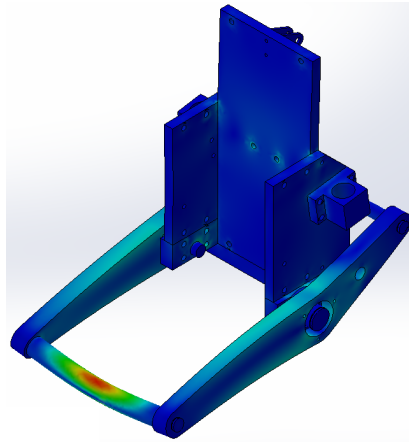
Figure 2.30: Illustrative example of one of the structural studies performed

When the anvil falls on the RCS, it can strike the arms before they are fully extended. Therefore, the methodology used was to perform several static studies, each with the arm in a different position of its course. Nine simulations were performed at nine equidistant points along the 30° course of the RCS's arms.

The point of maximum stress along the entire structure predictably happens in the middle of the impact axle, more specifically on its underside. After the 9 simulations were run, a graph was plotted with the results, fig. 2.31. From the graph, it is possible to see that the situation of highest stress for the system is the one where the arms have just barely lifted off the table of the machine and are essentially still in the resting position. The value of this stress at this point is 78.06 MPa, well below the yield strength for CK45 steel (530 MPa [28], for the impact axle and other steel parts) and Aluminium 6061 (255 MPa [29], for the aluminium plates and parts).
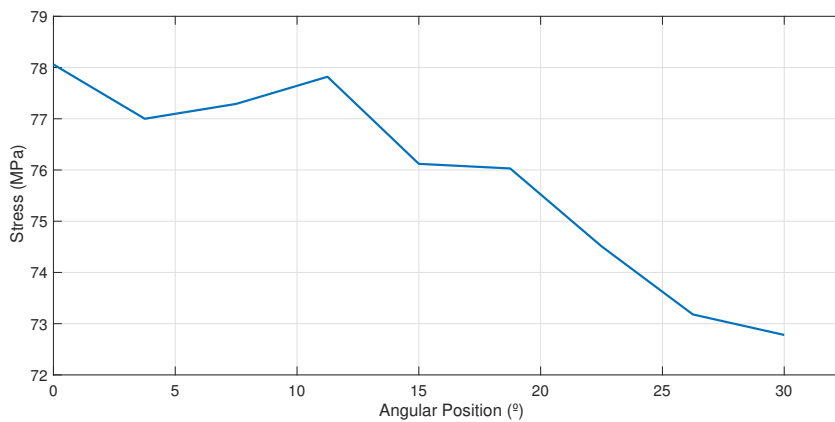
Figure 2.31: Maximum stress as a function of angular position of RCS arm

With the structural simulations complete, it was possible to conclude the design of the RCS. All the components have been designed, the functional simulations have been run and have verified that actuation time of the system is short enough, and the structural simulations have guaranteed that the RCS will be able to withstand the full force of impact of the anvil, and all the associated stresses.

Chapter 3

Electronics and Command Logic

In this chapter, the design of the electric system is discussed, ranging from the selection of the main components, to the design of the electric circuits for the machine.

The command sequence is also explained in this chapter going into detail with the various subroutines involved in the functioning of the machine.

3.1 Electronics

The machine, in order to be able to function, requires an electrical system. This system is responsible for powering the various components, as well as for providing the interface between the computer and the set of actuators and sensors. One of the major components of this thesis was to design, build and implement this electric system. This system can be divided into seven parts, each discussed in its own subsection:

- Velocity Acquisition Subsystem;

- Detectors;

- Lifting motor control;

- Pneumatic valve control;

- Signal acquisition and conditioning;

- Power circuit;

- Emergency circuit;

In this section, references to specific relays (such as `K1` and `K2`), signal lines (such as `PCIN3` and `PCOUT4`) and DAQ board ports (such as `PortA5` and `PortB6`) will be made. In order to comprehend their context and implementation, it may be helpful to consult the electric circuit diagrams in appendix A.

3.1.1 Velocity Acquisition Subsystem

While it is possible to give an estimate for the velocity of the anvil at the moment of impact given its drop height using $v = \sqrt{2g \cdot h}$ (where v is velocity, g is the acceleration of gravity and h is the drop height), this is only a theoretical estimate. In reality, effects such as air resistance alter the velocity at which the impactor strikes the sample, and thus, alters the impact energy, which can lead to skewed test results.
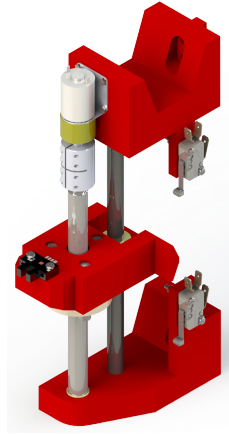
Figure 3.1: Velocity Acquisition Subsystem [5]

To fix this problem, the machine has a velocity acquisition subsystem installed, designed by Ramos [5] (shown in fig. 3.1). It works by having a specially designed two-pronged comb attached to the anvil, which passes through an optical interference detector (see section 3.1.2.3) as demonstrated in fig. 3.2. The second prong of the comb interrupts the detector's beam slightly after the first, and with that time difference and the distance between the combs, it is possible to determine the real velocity of the falling anvil.
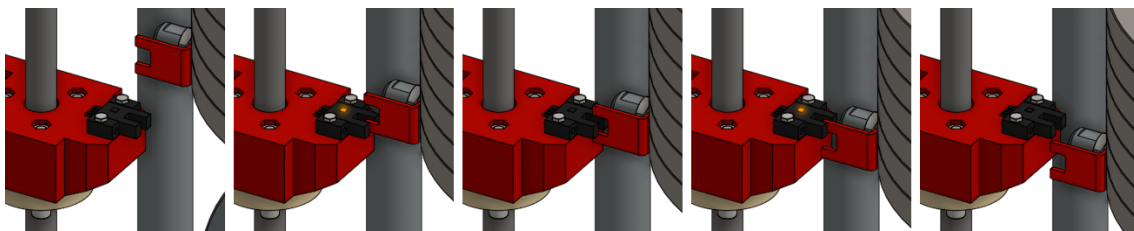
Figure 3.2: Working principle behind the Velocity Acquisition Subsystem as the anvil falls. Orange light represents a positive signal

Given that this machine can be used for a myriad of tests using many different kinds of samples, the vertical position at which the impact point lies can change. For this reason, it is important to be able to move the detector in the velocity acquisition subsystem to the desired reference point, and thus, there is a small DC gearmotor that connects to a screw drive which moves the

detector up or down according to the impact point. This motor chosen by Ramos is a Como Drills 918D100112 [5][30].

To be able to reverse the direction of this motor, Ramos [5] proposed a circuit based on the common H-Bridge motor controller that electronically reverses the polarity of the motor's power lines. This sort of circuit is perfect for the task since it allows for easy reversal of direction in a very simple and compact manner. On the other hand, producing the exact circuit proposed by Ramos would entail having to fabricate a custom-made PCB board for the task. To avoid this, a commercial alternative for this circuit was implemented. The board chosen was one built around the L298N (see fig. 3.3).
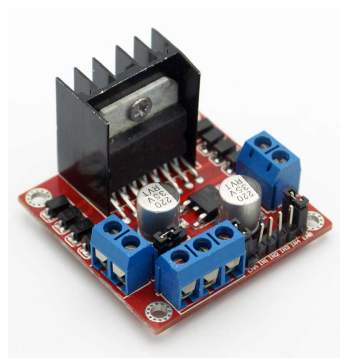
Figure 3.3: L298N motor controller

This is an integrated circuit that contains all the circuitry required for two complete H-Bridges [31] (though only one is needed), and is widely used in making DC motor controllers for small motors. The board, besides having the L298N integrated circuit, also contains protection circuits and voltage regulators. The board originally comes prepared to be used in conjunction with 12 V motors, but a jumper in the circuit can be removed to change the mode and have the board accept 24 V motors. The manufacturer, however, ambiguously named the port `12V` which can cause some confusion.

The board has a series of inputs and outputs, their description and signal lines are given in table 3.1.

Table 3.1: L298N board pinout, ignoring possible connections for a second motor

Pin Name	Line	Description
GND	GND24	Board ground
5V	5VDC_PS3	5 V supply
12V	24VDC_PS1	24 V supply
ENA	PortB0	Enable, motor only moves when active
IN1	PortB7	Direction selector
IN2	PortB6	Direction selector
OUT1	-	Motor power line
OUT2	-	Motor power line

3.1.2   Detectors

There are currently four sensing elements installed on the machine: an inductive detector, a photoelectric detector, an optical detector and two micro-switches. Each of them performs a different and very specific function in the machine, discussed in this subsection.

3.1.2.1   Inductive Detector

The inductive detector, an RS Pro 701-8253 [5][32] (see fig. 3.4), is installed in the carriage and has the function of acting as a limit switch to prevent the motor from elevating it beyond the upper limit of its course. A small piece of threaded rod is attached to the inside of the structure in such a way that when the carriage passes next to it, it is within the detection range of the detector and it sends a signal to the software (through line `PCIN5`). As an extra precaution, it automatically triggers a normally-closed relay (`K8`) and cuts power from the motor in order to make sure it really does not go past its limit.

Figure 3.4: RS Pro 701-8253 [32]

This extra precaution had one major issue that needs to be resolved: when the power is cut to the motor, the detector stops in front of the threaded rod. If the software tries to tell the motor to come back down, since the inductive detector is cutting the power from the motor, it will be unable to do so—it will be permanently stuck. This implies that a detector bypass must be installed. This comes in the shape of a parallel normally-open relay (`K9`) that is triggered by a signal given by the software (through line `PCOUT5`).

3.1.2.2   Photoelectric Detector

During normal operation of the machine, when it has gone through the anvil grabbing stage, the software needs a way of knowing whether or not the anvil has been successfully attached. This is the function of the photoelectric detector: it attaches to the underside of the carriage and detects whether the rod of the anvil is crossing its field of vision and uses this to determine its state of attachment.

The photoelectric detector chosen by Ramos [5] is an OMRON E3FA-DN23 [33] (see fig. 3.5).
This is a diffuse reflection detector, meaning it emits a light and it gives a signal whenever it detects
that same light being reflected back by an object that passes in front of it.

Figure 3.5: OMRON E3FA-DN23 [5]

The specific model of detector chosen for this function has an NPN configuration. If it were
PNP, the signal could be directly obtained from one of its leads and fed into the signal conditioning
circuit (much like the inductive detector), but this not being the case, there needs to exist extra
circuitry to take care of this detection using a relay (K11), shown in fig. 3.6
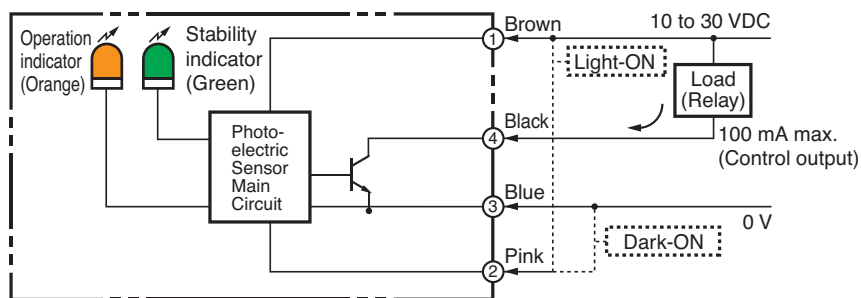
Figure 3.6: Photoelectric electric diagram, as proposed by OMRON [33]

The detector has four leads, identified by colours, stated in table 3.2. The pink lead can select
Dark ON or Light ON behaviour by being connected to the blue or brown leads, respectively. In
order to obtain a signal from the detector, the black lead (collector) is connected to the negative
lead of the relay coil and the brown lead (24 V) is connected to the positive lead of the coil. The
signal to be fed to the computer (line PCIN6) is then connected to a normally closed contact of this
relay. When the detector triggers, it allows current to flow through and power the relay, commuting
the contact. This system relies on the detector being configured to Dark ON mode.

Table 3.2: Photoelectric and optical detector lead colors

Pin Color	Description
Brown	24 V supply
Black	Collector
Blue	Emmitter/Ground
Pink	Dark ON/Light ON selector

3.1.2.3 Optical Detector

The optical detector, as mentioned in section 3.1.1 is used to measure the real impact velocity of the anvil during tests. This detector is an OMRON EE-SX670-WR 1M [5][34] (see fig. 3.7), a slot-type photomicrosensor. It works on the same principle as a light barrier: by having a light beam shine between an emitter and a receiver, and whenever that beam is interrupted, a positive signal is sent from the detector.

Figure 3.7: OMRON EE-SX670-WR 1M [5]

Much like the photoelectric detector, this detector was also acquired in an NPN configuration. Therefore, its installation and circuit diagram are identical to the one discussed in the previous section, requiring another relay (`K12`) to be used to extract a signal from the detector. Being very similar detectors with similar functionality, the lead colours and wiring is the exact same (see table 3.2).

Currently, an electromechanical relay is installed on the machine for this purpose, due to easy availability. Since the RCS is still not installed, the machine can not perform tests with too high a drop height, since without something to dissipate the impact energy, damage could be done to the machine's structure. A consequence of this is that the velocity at which the impactor hits the sample is generally slow enough that the relay is able to respond fast enough. When the RCS is installed and the machine is able to be used to its full potential, however, the relay being electromechanical will not be able to respond fast enough and should be replaced with a solid-state relay or similar electronic equivalent.

3.1.2.4 Micro-Switches

As described in section 3.1.1, the optical detector can be moved up and down through the use of a motor and a screw-drive. Since the movement has a limited course, implementing two limit switches is essential. This is the purpose of the two micro-switches.

The model of micro-switches implemented in the velocity acquisition subsystem is the Cherry D459-V3RD [5][35] (fig. 3.8). When pressed, the switches need to perform two actions: stop the velocity acquisition subsystem motor in the direction of the switch and send a signal to the computer so that the software can handle the situation.

b

Figure 3.8: Cherry D459-V3RD [5]

This model of switch is a 3-way switch, meaning that it has two contacts (one normally-open and one normally-closed) with a common input. When it is pressed, it commutes conduction between these two different contacts. This fact is used to perform both functions described above. The normally-closed contact is connected directly to a line that will input to the computer (`PCIN2` and `PCIN3` for ascending and descending movements, respectively), while the normally-open contact is connected to a relay that cuts power from the relevant line to stop movement (`K5` for ascending movement and `K6` for descending movement). Since each switch only cuts power from ports `IN1` and `IN2` of the L298N board and not the power from the motor itself, the motor can always move freely in the opposite direction, away from the limit switch.

3.1.3 Lifting Motor Control

One of the most important parts of the machine is the lifting subsystem, shown in fig. 3.9. Like the name implies, this subsystem is responsible for lifting the carriage with the anvil, whether to a specific height for testing or through manual speed control.
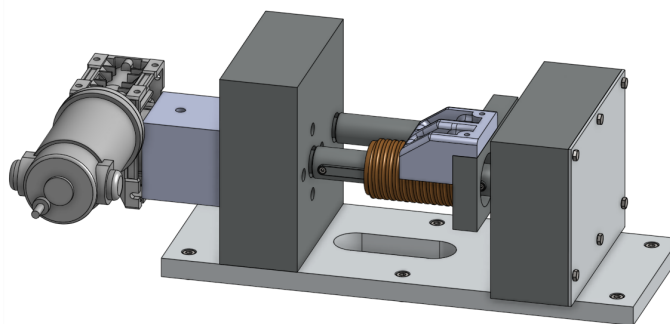
Figure 3.9: Model of the Lifting Subsystem. Helical barrel shown in orange

The mechanical solution for this subsystem was proposed by Castro [11] and later modified and implemented by Ramos [5]. It consists in having the carriage attached to a cable that is pulled by wrapping around a motorised pulley. In order to maintain a constant velocity throughout the whole course of the lift, the pulley's radius needs to remain constant. If the pulley were a

simple drum, the cable wrapping around it would increase the radius as the height of the carriage increased, so instead, a solution using a helical barrel was implemented. This guarantees that no matter the position of the carriage, the relation between motor velocity and carriage velocity is kept constant.

The actuation of the lifting subsystem is taken care of by a DC worm gear motor. This motor, as chosen by Ramos [5] is a Transtecno ECM-100/040 [36] (fig. 3.10a).

In order to control this motor, a drive was also chosen by Ramos [5], namely, an Electromen EM-12A [37] (fig. 3.10b). This is a PWM drive that converts a reference signal into the adequate voltage signal to rotate the motor at a given speed. This drive accepts several ways of receiving the reference signal:

- Potentiometer control;

- Potentiometer control with forward/reverse switch;

- Forward/reverse switch at predefined velocity;

- External $\pm 10\,\text{V}$ reference.
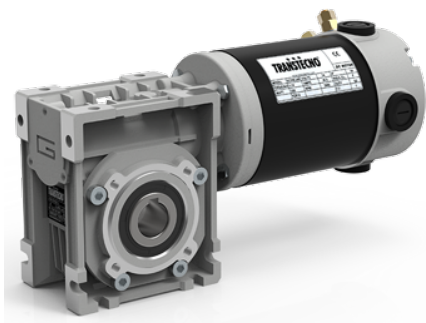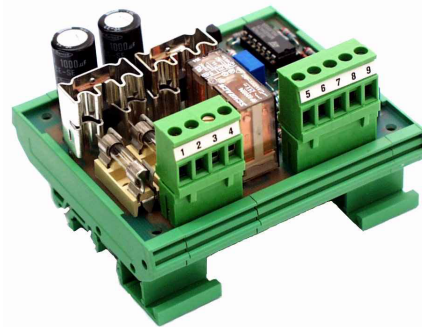
(a) Transtecno ECM-100/040 [36]   (b) Electromen EM-12A [37]

Figure 3.10: Lifting motor and respective drive

Given that the machine will be connected to a computer with a DAQ board with analog outputs (see section 3.1.5.1), the easiest and best way to provide the reference signal is the latter option, to connect directly to an external $\pm 10\,\text{V}$ reference provided by an analog output channel on the board. With this set, and taking emergency circuitry into consideration, it was possible to design the circuit diagram for the motor, shown in appendix A.

The motor also comes equipped with an encoder, though its implementation is discussed in section 3.1.5.2.

3.1.4   Pneumatic Valves

Currently, in the machine, only one pneumatic actuator is installed (in the carriage for anvil release). However, in the future when the RCS is implemented, two further pneumatic actuators will

be installed (as discussed in chapter 2) so when designing the electronic circuit, this was taken into account, and everything was designed as if the actuators were already a part of the machine, to prevent the need for a future redesign of the electronic system.

(a) SMC C85N25-25S [5]   (b) Parker B3R5BXXXXH [5]

Figure 3.11: Release mechanism cylinder and its valve

The actuator installed in the anvil release mechanism is an SMC C85N25-25S [38], chosen by Ramos [5] (fig. 3.11a). To go along with this actuator, Ramos [5] also selected a valve, the B3R5BXXXXH from Parker [39] (fig. 3.11b). However, this valve did not come with a solenoid, so that had to be selected as well. The selected solenoid was the P2E-KV32C1 [40] also from Parker.

Though there are three actuators, two of them, from the RCS, will always act in parallel, so in reality, only two signals are needed from the computer: One for the anvil release (line `PCOUT1`), and another for RCS activation (line `PCOUT2`). These signals will activate relays which in turn will power the solenoids that commute the valves and cause the actuators to extend. With this in mind and considering the emergency circuitry, the circuit diagram for the valves was designed.

3.1.5 Signal Acquisition and Conditioning

The control of the machine is via software, namely, through a program designed in Simulink® and `MATLAB`®. Therefore, there needs to exist a way for the detectors and actuators to communicate with the computer where the software is running on. In order to do this, a DAQ board was installed on the PC. This board, as well as the computer, works with 5 V digital logic, unlike the machine that mostly works with 24 V. For this reason, a circuit board had to be designed that was able to convert the 24 V signals coming from the machine electronics into digital 5 V signals and 5 V signals coming from the computer into 24 V signals for the machine. Finally, and also discussed in this subsection, the motor responsible for the lifting subsystem (see section 3.1.3) contains an encoder which needs to be read by the computer. A second board was also chosen and installed on the computer to collect the data from the encoder and decode it into information about its position so that the software can interpret it.

3.1.5.1 DAQ Board

The chosen DAQ board was a PCIM-DDA06/16 from Measurement Computing [41], shown in fig. 3.12. This board is ideal since it has two types of ports, six analog output channels as well as twenty-four bits of digital I/O [41], both of which are required for the motor control and detector input.

Figure 3.12: Measurement Computing PCIM-DDA06/16 [41]

The 24 bits of digital I/O are divided into 3 channels, A, B and C, each one containing 8 bits, making one byte. Each channel can be individually set as an input channel or an output channel, but individual bits may not. Hence, when deciding how to connect the bits to the different detectors and actuators, it was necessary to take this into consideration and group everything accordingly. Channels B and C were set as output channels, and A was set as an input channel. The different lines for each digital channel are shown in table 3.3. One analog output (`AOUT0`) is also used to control the lifting motor.

Table 3.3: DAQ digital I/O port signals

Channel	Bit	Line	Description
A (Input)	A2	PCIN6	Optical detector signal
	A3	PCIN4	Photoelectric detector signal
	A4	PCIN5	Inductive detector signal
	A5	PCIN3	Velocity acquisition subsystem lower limit switch
	A6	PCIN2	Velocity acquisition subsystem upper limit switch
	A7	PCIN1	Emergency switch signal
B (Output)	B0	ENA	L298N Board Enable
	B1	PCOUT5	Inductive detector override
	B2	PCOUT4	Velocity acquisition motor power supply
	B3	PCOUT3	Emergency signal from computer
	B4	PCOUT2	RCS activation
	B5	PCOUT1	Anvil release signal
	B6	IN2	Velocity acquisition subsystem motor, ascending motion
	B7	IN1	Velocity acquisition subsystem motor, descending motion
B (Output)	C0	INDEX	Encoder reset

3.1.5.2 Encoder and Encoder Board

In order to determine the position of the carriage, the lifting motor is equipped with an optical encoder, specifically an ME22-300-6.000-2LS1 by Intecno [42], a high-resolution optical encoder. The encoder has 3 channels, A, B and I. Channel A gives a pulse every time the encoder turns a certain angle (calculated below) and Channel B gives the same pulse phase shifted by half that angle. This is used to determine the direction in which the motor is turning. Channel I or Index, gives a pulse every full rotation, but it will not be used. The pulses are all illustrated in fig. 3.13.
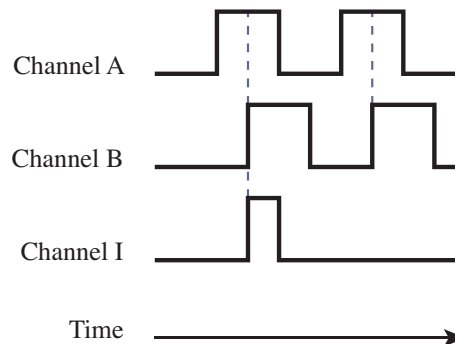
Figure 3.13: Encoder signals during constant rotation as a function of time

To interpret the pulses from the encoder and turn them into information regarding the position of the motor shaft, a quadrature encoder board was used. The one chosen was a PCI-QUAD04 by Measurement Computing [43], shown in fig. 3.14. Being a quadrature board, it can not only read the rising edge of the pulses but also the falling edge. This, in turn, means that it can read 4 signals per count of the encoder, which multiplies the resolution by four. The encoder manual states the resolution of the encoder to be 300 counts per revolution, but with quadrature, the effective resolution becomes $300 \times 4 = 1200$ counts per revolution.
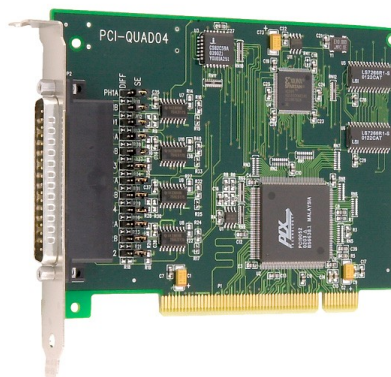
Figure 3.14: PCI-QUAD04 board

Simulink®, where the software is designed, possesses a block designed to interpret input from a PCI-QUAD04 board. One thing it lacks, however, is a way of resetting the encoder at will,

which can be helpful at times, for example, before positioning the carriage when starting a new test. A way around this is to use the option to reset the count every time the Index of the encoder is activated, but instead of connecting the actual index of the encoder, connect a signal from the DAQ board (`C0`) that can be triggered at will and will reset the encoder count in Simulink®.

3.1.5.3 Signal Conditioning Board

As mentioned in the beginning of section 3.1.5, a PCB board had to be designed in order to convert the 24 V signals coming from the machine's electronics into 5 V signals that the DAQ board can receive, and vice-versa. There are many approaches one could take to perform this task, but the best solution that was found involved using optocouplers. These components are similar to relays, in that they have two separate, isolated lines, and the current passing through one line (in the relay analogy, the current passing through the coil), triggers current flowing through the other (the contact of the relay). In the case of optocouplers, the coil is replaced by an LED and the contact is replaced by some sort of phototransistor. When current flows through the LED, it lights, and the phototransistor closes the circuit, allowing for current to flow freely through that line. This is very useful, since it electrically isolates both lines, meaning there can never be any bleeding of the 24 V signal into the computer, which could damage its internal circuitry. The specific optocoupler used was a PS2502-4, a small integrated circuit containing 4 individual optocoupler circuits, allowing for multiple lines to be connected at once, as depicted in fig. 3.15.
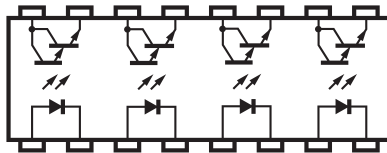
Figure 3.15: PS2502-4 schematic symbol (adapted from [44])

Since the board needs to convert the signals both ways, there are two circuits to be designed, one for inputs to the computer, and one for outputs from the computer.

The circuit for the computer inputs is shown in fig. 3.16: 24 V line `PCIN6` needs to trigger bit `A2` on the DAQ board. In this circuit, the only components that need to be dimensioned are the resistances, using Ohm's and Joule's laws.

Applying Ohm's law to line `PCIN6` we get:

$$\Delta V_{R1} + \Delta V_{LED} = I \cdot (R_1 + R_{LED}) \tag{3.1}$$

where ΔV_{R1} is the voltage drop of resistance `R1`, ΔV_{LED} is the voltage drop across the LED of the optocoupler, I is the current flowing through the components and R_1 and R_{LED} are the resistances of `R1` and the LED respectively. The resistance of the LED will be very small when compared to R_1 so it can be safely ignored. The voltage drop across the LED is stated in the datasheet of

Figure 3.16: Computer input conversion circuit for a single line (PCIN6 to A2)

the PS2502-4 integrated circuit as having a typical value of $1.17\,\text{V}\,@\,10\,\text{mA}$ [44], but it is variable. Thus, the worse case scenario for calculating R_1 will be considered, namely, when $\Delta V_{LED} = 0\,\text{V}$. Therefore, equation 3.1 becomes:

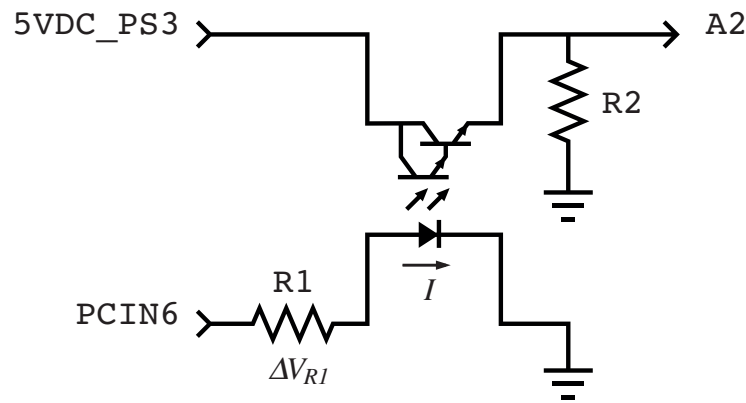$$\Delta V_{R1} = I \cdot R_1 \tag{3.2}$$

The minimum current for the LED to function is stated to be $10\,\text{mA}$ in the datasheet [44], so in order to stray from the minimum, a current of $20\,\text{mA}$ is chosen. Therefore, according to equation 3.2, $R_1 = 1200\,\Omega$. Using Joule's law, it was also possible to calculate the power the resistance needs to have in order to not burn out.

$$P_{R1} = I \cdot \Delta V_{R1} = \frac{\Delta V_{R1}^2}{R_1} = 0.48\,\text{W} \tag{3.3}$$

where P_{R1} is the power rating of resistor R1. So therefore, the normalized resistor implemented was a $1.2\,\text{k}\Omega$, $1/2\,\text{W}$ resistor.

Resistor R2 is a pull-down resistor: it prevents a "floating" tension value when current is not flowing through the 5 V line and guarantees a 0 V tension in order to stop false positives. The values for pull-down resistors don't need to be necessarily calculated since they don't have much current flowing through them, instead, experimentation proved $390\,\Omega$ to be a good value for the resistance of R2, with a $1/8\,\text{W}$ power rating.

The circuit for the computer outputs is shown in fig. 3.17. This circuit is very similar to the previous, but it has no need for a pull-down resistor and it controls the respective relay through the negative pole, and not through the positive. In order to facilitate, the same resistors used for the pull-down were used for this circuit as well, which gives a value of current of $12\,\text{mA}$.

Having designed the circuit for individual lines, it is simple to extend it to include all the inputs and outputs required. Due to the number of ports to convert to and from, four PS2502-4 integrated circuits were used, two for converting inputs and two for converting outputs. Once the circuit was designed, a schematic was imported into a PCB design software, and the actual
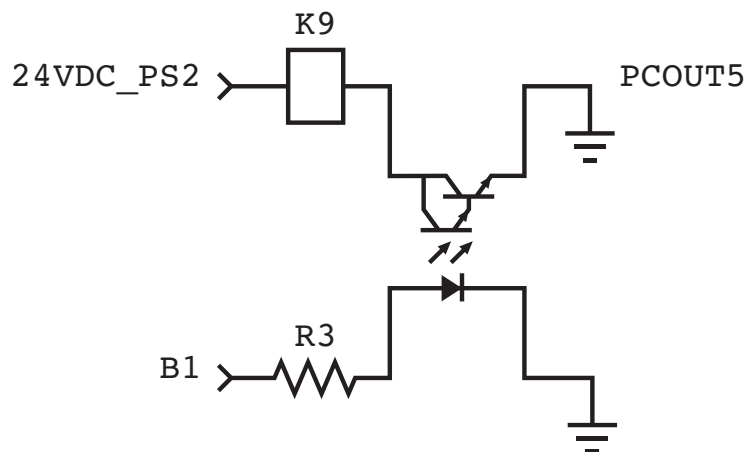
Figure 3.17: Computer output conversion circuit for a single line (`B1` to `PCOUT5`)

PCB board was drawn. To do this, it was necessary to draw every copper line that will be present on the final board and to make sure that there are no crossovers, short circuits or small gaps between lines where solder or electrical arcing could cause problems. Due to limitations in the PCB manufacturing process available, only one layer of copper could be etched, which made things difficult, but fortunately, the topology of the circuit still allowed it to be designed in one layer only, but only after much trial and error. The files were then exported into a *gerber* format that could be used to fabricate the final PCB board through a chemical etching process. A diagram of this file is shown in fig. 3.18.

Figure 3.18: PCB design file in *gerber* format

3.1.6 Power Circuit

The power source for the machine is obtained directly from the mains and therefore comes in the form of AC current. In order to convert the power to DC and guarantee the desired voltage levels, power supplies are used. Since there are no analog signals with the exception of the drive reference (which is generated by the DAQ board), ther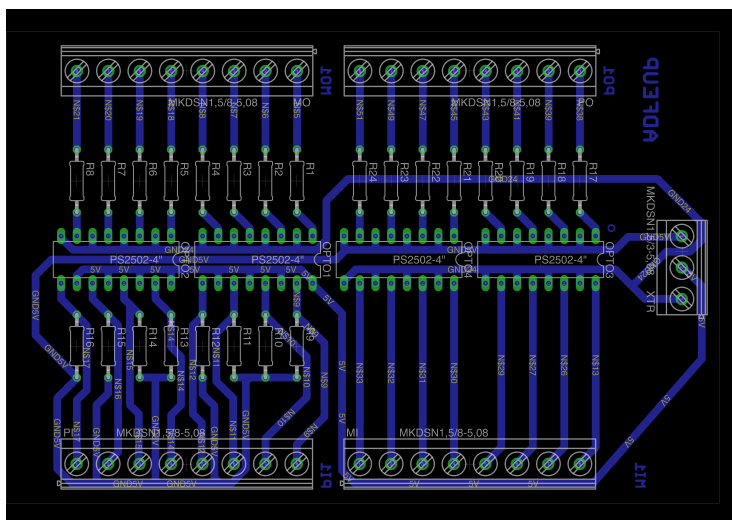e is no issue with power supply noise. Therefore, switch power supplies can be used instead of linear power supplies, since they are significantly cheaper.

The electrical system contains 3 power supplies:

- PS1 – 24 V power supply for the lifting motor;

- PS2 – 24 V power supply for the rest of the relays and detectors;

- PS3 – 5 V power supply for the signal conditioning board and for the L298N board.

Since the lifting motor has such a major role in the machine and requires a lot of power, it was decided to provide it with its own power supply. The lifting motor is a 24 V, 140 W gear motor. Therefore, at max power, the current it will require can be calculated as:

$$P = I \cdot V \implies I = \frac{140}{24} \approx 6 \, \text{A} \tag{3.4}$$

In order to guarantee enough current was actually available and since 24 V power supplies with 6 A were not available, a 10 A power supply was chosen, namely an RS Pro 240W DRP-240 Series [45] (fig. 3.19a). The other 24 V power supply is calculated by adding up the current required by every other electronic component in the system and estimating a final value for the current required. The final estimation with some extra current for safety added up to 4 A, so an RS Pro 96W MDR-100 Series was selected (fig. 3.19b).

(a) RS Pro 240W DRP-240 Series [45]

(b) RS Pro 96W MDR-100 Series [46]

(c) RS Pro 10W MDR-10 Series [47]

Figure 3.19: Power supplies

The third power supply is a 5 V one. It will mostly need to provide power to run the velocity acquisition motor, but also the signal conditioning board and the L298N board, which will also

require some current. When added up, the total current required will be very little, so a 2 A power supply was chosen, which is more than enough for the components. The power supply model chosen was an RS Pro 10W MDR-10 Series [47].

Finally, like in all electronic machines, some circuit protections had to be implemented, such as a general power switch, circuit breakers (or a fuse in the case of the 5 V power supply), and a residual-current circuit breaker.

3.1.7 Emergency Circuit

When designing any machine, it is very important to take into consideration all the things that can go wrong, minimise the risk of them ever happening, and in the case where they do happen, implement a way to stop them. This machine is no exception.

Currently, there are only two triggers that will make the machine enter an emergency state: an emergency button is pressed, or the anvil carriage hits the upper limit detector. On the other hand, the machine is still not complete. In the final version of the machine, when safety barriers are installed, for example, other emergency cases will be able to be detected such as if the barriers are opened when they shouldn't be.

The machine has three emergency buttons: One installed on the machine's structure itself, one next to the computer (fig. 3.20), and one virtual button, for redundancy. The reason for this is that the user can be either working directly on the machine (for example, when changing the tool or the test sample) or working on the computer, on the interface.

Figure 3.20: Schneider Electric Emergency Button XALK178E

The effect of the emergency state is to immediately cut power from the various actuators to stop the lifting motor and the velocity acquisition motor, as well as the anvil release cylinder. The RCS actuators, however, should behave in the exact opposite way: since they are a safety system, they should trigger and activate immediately. A signal should also be sent to the computer in order to inform the software that an emergency state has been initiated.

In order to perform these actions, activating the emergency buttons triggers relays: `K3` in the case of the physical buttons (shown in fig. 3.20), `K4` in the case of the digital button. These relays have normally closed contacts in series with the power lines of the various components that need to have their power cut. The RCS actuators, however, have normally open contacts in parallel.

This way, it is guaranteed that even in the software freezes, there is no possible movement allowed for the components.

The software is always listening to the emergency trigger and no matter the state the program is in, it can at any moment switch into an emergency state. After entering this state, it waits for a user input and enters a manual emergency mode where power is returned to the various components but no tests can be performed. This is further discussed in section 3.2.6.

3.2 Command Sequence and Logic

As stated, the command sequence of the machine is controlled by a program running in Simulink® on a computer connected to the machine. This program uses the Simulink Real-Time™ toolbox to connect to the DAQ and encoder boards and the Simulink Stateflow® environment to design the various states and transitions of the machine behaviour. A command sequence had already been created by Ramos [5], but while parts of it were implemented in the final product, many of the sequences had to be changed for various reasons. Ramos also proposed many subroutines that were not developed in detail, so those had to be designed as well. The command sequence developed in this thesis does not include the RCS, since it is still not present.
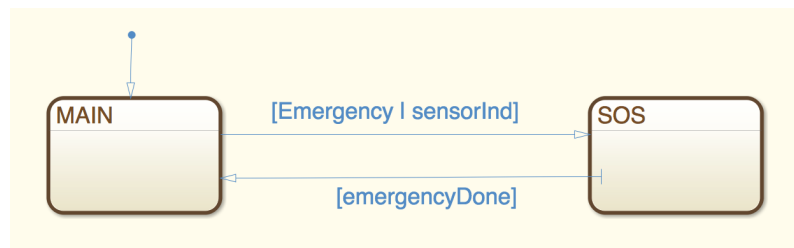

Figure 3.21: Example of two states and two transitions between them

The Simulink Stateflow® environment allows for easy programming through state machines. Each state is represented as a block that can perform actions, and between different states transitions can be defined, which are boolean functions that trigger when they equate a `True` value. This is exemplified in fig. 3.21. The Simulink Stateflow® environment can be accessed in Simulink® through the use of a Chart. Charts are blocks that receive inputs from the Simulink® block diagram, run the state machine, then return outputs right back to the Simulink® block diagram in real time. Charts can also contain internal, local variables for use in the state operations and actions that do not influence the block diagram on the outside. A list of variables can be found in appendix B, for reference.

States can perform actions by themselves and those actions can be divided into three categories:

- `entry` – Action that is performed on entry into the state;

- `during` – Action that is performed while the state is active;

- `exit` – Action that is performed as the state becomes inactive.

States, besides the actions they can perform by themselves, can also contain other state machines inside, that run when the parent state is active, effectively allowing for the creation of subroutines. This fact is used to make the program easier to understand, and more modular—similar subroutines are defined and used throughout the program in order to facilitate implementation, instead of having to repeat everything. Transitions between parent states always take precedence over transitions within internal states, meaning if a transition happens from a subroutine to a different state, the elements of the subroutine all cease to be active and stop any actions they are performing.

In the following subsections, an overview of the program is given, starting with the general overview of the whole state machine, and then going into detail with the various subroutines. Each subsection details one specific subroutine and may also include some minor internal subroutines as well.
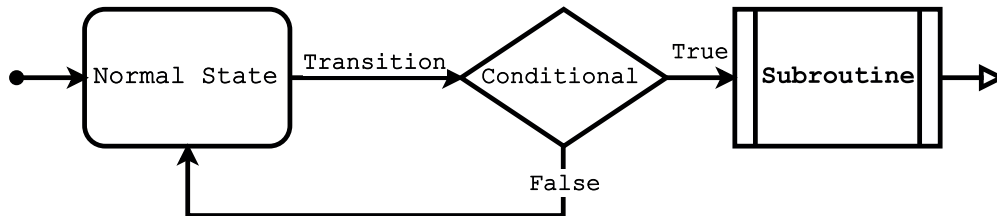

Figure 3.22: Reference for state diagrams

In fig. 3.22 is presented a legend to aid in the interpretation of the state diagrams. It shows a normal state, a subroutine, a conditional block and a transition, but also a "start" transition as an arrow with a circle, and an "end" transition as a white arrow. The state diagrams presented will not show the actual code, but instead a simplified "pseudocode" in order to convey the functioning of the different subroutines in a more understandable fashion.

3.2.1   General Overview and `MAIN` Subroutine

Figure 3.23: Highest-lever routine
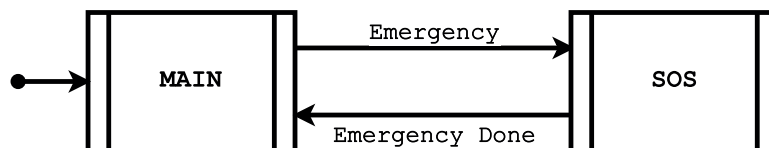
The highest level of the state diagram, shown in fig. 3.23, only contains two states: the `MAIN` state and the `SOS` state. These correspond to the normal functioning of the machine, and the emergency state, respectively. The reason why this is done in such a way is to guarantee that the program is always ready to enter into emergency, since as mentioned, the transitions of the parent

state always take precedence over the transitions of the child states of the subroutine. Given that all of the normal functioning of the machine rests inside the MAIN state, an emergency signal will always take precedence and cause the SOS state to become the currently active state.

The rest of this section will concentrate on the MAIN subroutine; the SOS subroutine will be discussed in section 3.2.6. As can be seen in fig. 3.24, the MAIN routine is comprised of four states:

- The INIT subroutine;

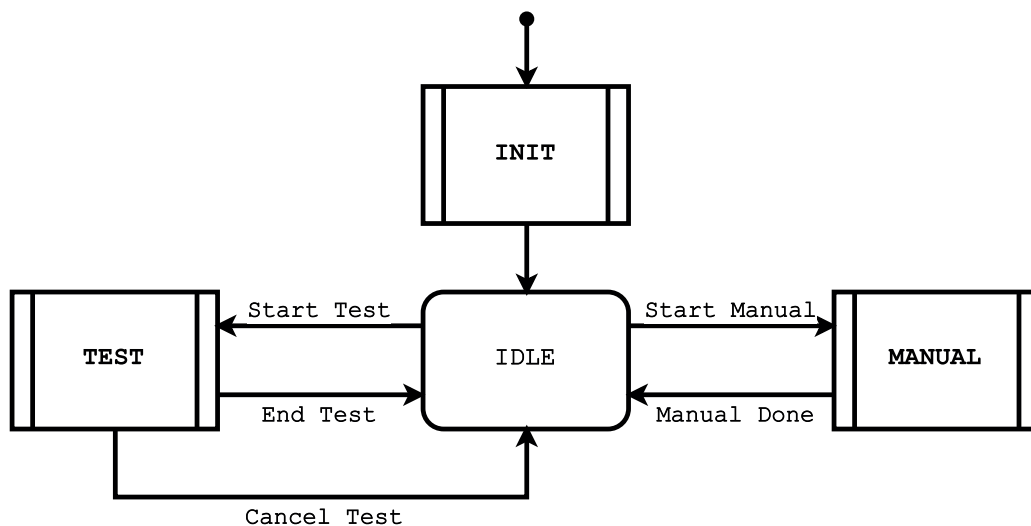- The IDLE state;

- The TEST subroutine;

- The MANUAL subroutine.

Figure 3.24: MAIN subroutine

The three subroutines, INIT, TEST, and MANUAL take care of the initialization of the program and the machine, the test sequence and the manual control sequence, correspondingly and will be discussed in later sections of this thesis. The IDLE state is, like the name implies, an idle state; it merely waits until input is given from the user to enter another subroutine. On entry, this block also ensures no part of the machine is moving by turning off all actuators. This is not really necessary, since the command sequence should never allow a transition into IDLE with an active actuator, but it acts as an extra layer of security. This is a new state previously not present in Ramos' control sequence.

3.2.1.1 INIT Subroutine

The INIT subroutine is also quite simple and composed of three blocks as shown in fig. 3.25. The Initialise Variables state initializes the variables of the program. The other two

subroutines, `FIND_VELAQ` and `CHECK_ANVIL` take care of positioning the velocity acquisition carriage in a known position (at the top of its course) and checking whether the anvil is attached to the carriage, respectively.

Figure 3.25: `INIT` subroutine

3.2.1.2 `FIND_VELAQ` Subroutine

The `FIND_VELAQ` subroutine is essentially a conditional statement, as shown in fig. 3.26. It checks whether the upper limit switch of the velocity acquisition subsystem is being pressed (`FDC_SUP`) and if not, moves its carriage up until it triggers said switch. As soon as the switch is triggered, it is guaranteed that the velocity acquisition subsystem carriage is at the topmost point of its course, which is desired, since it will save time in a future routine in the `TEST` subroutine (`Position Zero`).
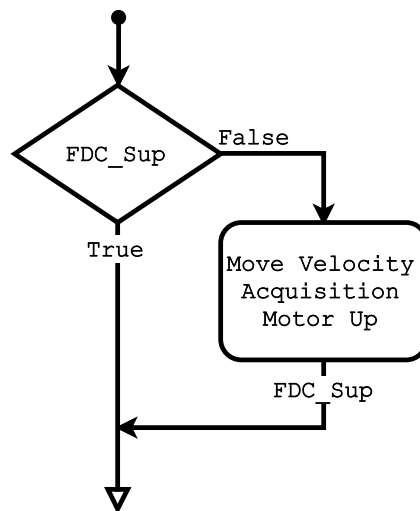
Figure 3.26: `FIND_VELAQ` subroutine

3.2.2 `MANUAL` Subroutine

The `MANUAL` subroutine, shown in fig. 3.27, allows for full manual control of the carriage, including release of the anvil. Ramos originally made a proposition for the `IDLE` state to be replaced by this subroutine and had different, separate subroutines for changing the mass, tool and test specimen [5]. However, upon consulting with the members of ADFEUP, who will be the end

users of the machine, it was concluded that this only complicates the user interaction and can even be somewhat limiting. The approach was then changed, and the "Change mass" and "Change tool/specimen" states proposed by Ramos [5] were abandoned. These changes are now taken care of by the user during the `MANUAL` subroutine, where the user has full control of the carriage and can change everything at will.
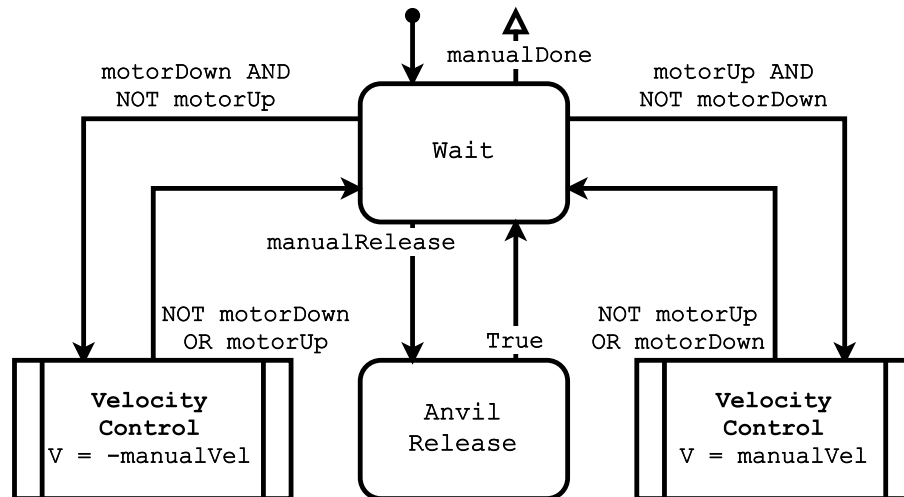

Figure 3.27: `MANUAL` subroutine

The `MANUAL` subroutine has a state (`Wait`) that, much like the `IDLE` state, just simply waits for an order from the user to perform an action. This order can take three forms. The first is from the inputs `motorUp` or `motorDown` and causes the motor to turn and bring the carriage up or down in velocity control. The velocity at which the carriage is moved is defined by the user in the interface and is carried by the variable `manualVel`. The second possible order comes from the input `manualRelease` and causes a signal to be sent to the anvil release actuator. Finally, the user could provide the input `manualDone`, signalling that there is an intention to stop the manual mode and return to the `IDLE` state.

When the motor is being moved up or down, it is constantly listening to whether the move (in that direction) order has been released, and if so, the active state returns to `Wait`. The same happens if the user tries to give orders to move in both directions at the same time.

3.2.2.1 `Velocity Control` Subroutine

When being controlled manually, the motor is controlled in velocity control instead of position control. Therefore, the program only needs to give a velocity reference to the drive, which will then take care of moving the motor at the corresponding speed. The user defines a unitless velocity level (ranging from 0 to 10, half the driver voltage range) in the interface which is then fed into the subroutine (variable `manualVel`). There is no point in having the user enter the actual speed that the carriage moves, since he/she will not have very good perception of velocity regardless and thus will treat both a unitless and a real velocity input in the same way.

If the user orders the motor to move up, the value given to the drive will be `motorVel`, if the order is to move down, `−motorVel` will be the value given.

3.2.3 `TEST` Subroutine

The `TEST` subroutine, shown in fig. 3.28, like the name implies, is the subroutine where tests are performed. Whenever it becomes active, it has already been through the `INIT` procedure, which in turn signifies that a verification of whether the anvil is attached to the carriage or not has been performed at least once (through subroutine `CHECK_ANVIL`). This implies that the system is aware of the status of anvil attachment, even if the user has been through the `MANUAL` state or has performed previous tests, since the program keeps constant track of whether or not the anvil has been released or reattached to the carriage in boolean variable `AnvilAttached`.
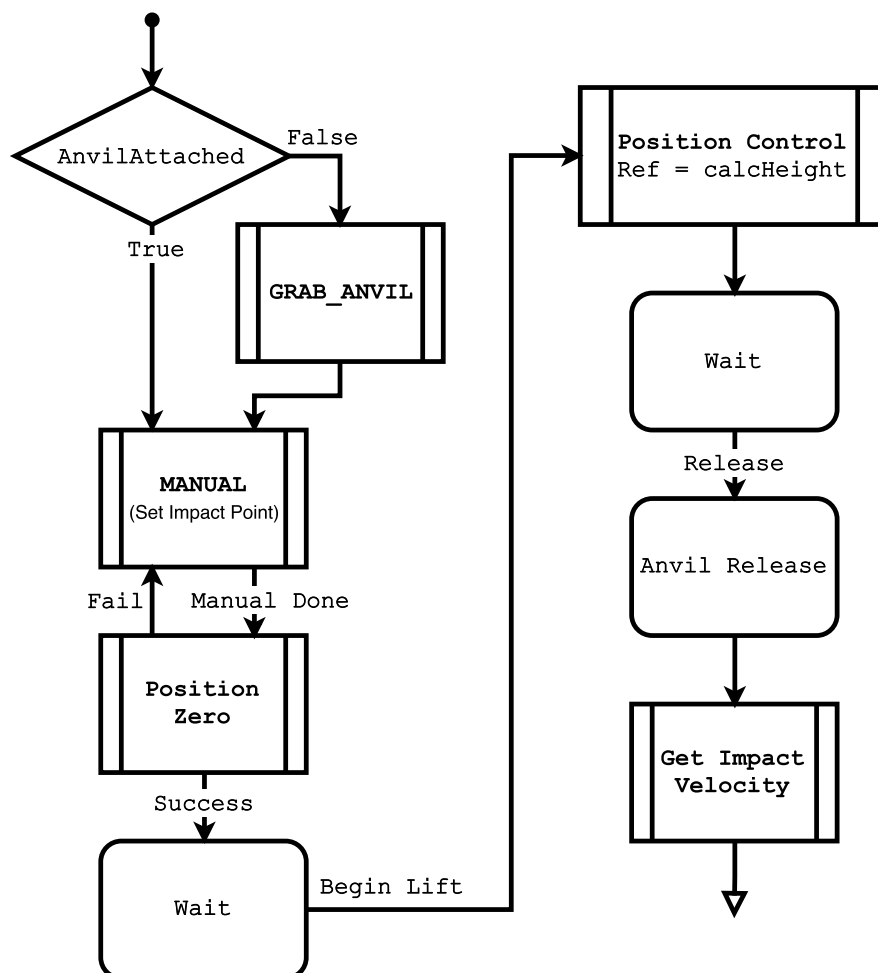

Figure 3.28: `TEST` subroutine

The first step in the `TEST` subroutine is therefore to check the `AnvilAttached` truth value to know if the anvil is attached or not, since the test can only be performed if it is. If so, the system

moves on, but if the anvil is not attached, it will initiate the GRAB_ANVIL subroutine, and only when there is absolute certainty that the anvil is attached does the program move on.

Once this step is performed, the impact point needs to be set. This is done in two parts: A MANUAL subroutine so that the user can place the impactor in contact with the test sample, and a Position Zero subroutine. This latter subroutine tries to move the velocity acquisition sensor such that it sits just above the anvil comb so that it can obtain the velocity as close to the moment of impact as possible.

Once the Position Zero subroutine has gone through successfully, the TEST subroutine will enter an empty state, simply waiting for an order to begin the lifting procedure of the carriage (subroutine Position Control) to the height calculated from the data given in the interface (input CalcHeight). Once the carriage has arrived at the requested height, the subroutine will once again wait for instructions, in this case in the form of an anvil release order (input testRelease). Once the release order is given, the anvil will begin falling and as soon as the anvil crosses the velocity acquisition sensor, it will trigger the subroutine to calculate the impact velocity (Get Impact Velocity).

3.2.3.1 `Position Zero` Subroutine

In this subroutine (fig. 3.29), the program moves the velocity acquisition carriage up until it hits the upper limit switch (rising edge of input FDC_Sup). This guarantees that no matter the position on the anvil, as long as it is in the course of the velocity acquisition subsystem, its carriage will stand above the comb. It will then proceed to move the velocity acquisition subsystem carriage down until the optical detector is triggered (rising edge of input SensorZero). When this happens, it signifies that the detector has reached the comb, and so the impact point has been set. The TEST subroutine can then move on through the Success transition. However, it may be the case that the anvil has not been correctly positioned inside the course of the velocity acquisition subsystem. In that case, when the velocity acquisition carriage moves down, it will never strike the anvil comb, and will instead strike the lower limit switch (rising edge of input FDC_INF). In that case, the subroutine will follow the Fail transition and will return to the MANUAL state so that the user can reposition the anvil correctly.
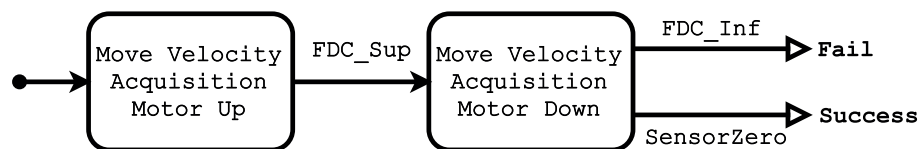

Figure 3.29: Position Zero subroutine

3.2.3.2 `GRAB_ANVIL` Subroutine

The GRAB_ANVIL subroutine shown in fig. 3.30 is the subroutine that allows the user to manually control the lifting and lowering of the carriage to grab the anvil. The weight of the carriage itself

is enough to make the clasping system of the carriage engage properly, so the user only needs to softly descend it onto the anvil.

After completing the MANUAL subroutine, it runs a CHECK_ANVIL subroutine to check whether the user completed the anvil-grabbing correctly.
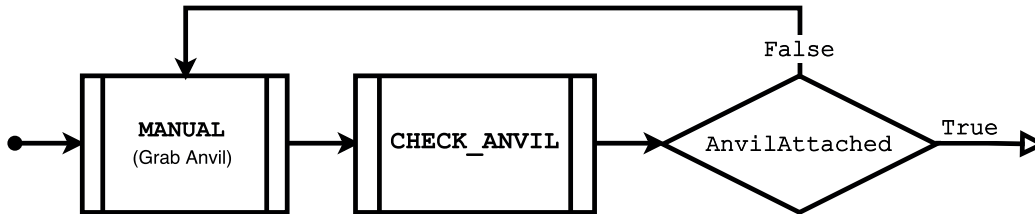
Figure 3.30: GRAB_ANVIL subroutine

3.2.3.3 `Get Impact Velocity` **Subroutine**

This subroutine is very important for the final results of the test, since it will be the one where the real impact velocity will be calculated, and hence the real impact energy. It takes input from the optical sensor as well as from a real-time clock, in order to calculate this velocity (variable realVel). This routine is shown in fig. 3.31.

Figure 3.31: Get Impact Velocity subroutine

When the anvil falls after being released, it will pass through the velocity acquisition subsystem. Its comb will trigger the signal two times, and the system will record both times from the real-time clock into the variables t0 and t1. Using those variables and the distance between

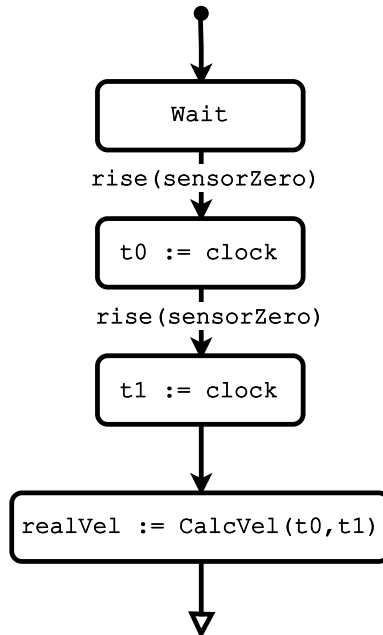prongs of the comb, `VELAQ_Dist`, it runs a function `CalcVel` to calculate the real velocity of the anvil.

The easiest way of calculating this value is to simply equate the impact felocity to the average velocity:

$$\texttt{realVel} = \frac{\texttt{VELAQ\_DIST}}{\texttt{t1} - \texttt{t0}} \tag{3.5}$$

This, however, does not take into consideration the fact that along the descent of the anvil, it accelerates slightly throughout its course. A correction can be made by also defining the average velocity in a more rigorous fashion:

$$v_{med} = \frac{1}{\Delta t} \cdot \int_0^{\Delta t} v(t) dt \tag{3.6}$$

where v_{med} is the average velocity, $v(t)$ represents the evolution of velocity as a function of time, and Δt is the difference of `t1` and `t0`. $v(t)$ can be approximated with having linear behaviour, and thus can be replaced by one of the fundamental laws of motion:

$$v_{med} = \frac{1}{\Delta t} \cdot \int_0^{\Delta t} (u + g \cdot t) dt \tag{3.7}$$

where u is the velocity of the anvil at the instant where it crosses the first prong. Thus, by solving the integral and equating the average velocity to the one calculated in equation 3.5, it is possible to solve for u:

$$\frac{\texttt{VELAQ\_DIST}}{\Delta t} = \frac{1}{\Delta t} \cdot \left(u \cdot \Delta t + \frac{1}{2} \cdot g \cdot \Delta t^2\right) = u + \frac{1}{2} \cdot g \cdot \Delta t \implies u = \frac{\texttt{VELAQ\_DIST}}{\Delta t} - \frac{1}{2} \cdot g \cdot \Delta t \tag{3.8}$$

Knowing u, it is then possible to calculate the impact velocity as:

$$\texttt{realVel} = u + g \cdot \Delta t = \frac{\texttt{VELAQ\_DIST}}{\Delta t} - \frac{1}{2} \cdot g \cdot \Delta t + g \cdot \Delta t = \frac{\texttt{VELAQ\_DIST}}{\Delta t} + \frac{1}{2} \cdot g \cdot \Delta t \tag{3.9}$$

and therefore:

$$\texttt{CalcVel(t0,t1)} = \frac{\texttt{VELAQ\_DIST}}{\texttt{t1} - \texttt{t0}} + \frac{1}{2} \cdot g \cdot (\texttt{t1} - \texttt{t0}) \tag{3.10}$$

After being calculated, this value is then sent to the interface, to be looked at by the user.

3.2.4 `CHECK_ANVIL` Subroutine

The `CHECK_ANVIL` subroutine, as mentioned in section 3.2.1, is the subroutine that checks whether the anvil is attached to the carriage. The photoelectric detector, being under the carriage can detect the presence of the anvil, however, it cannot detect if the anvil is attached or if the carriage is

hovering above the anvil, with it still in range. Thus it is necessary to have a routine to be sure of the status of attachment.

As shown in fig. 3.32, this subroutine begins with a conditional block: is the detector on? If not, the anvil is clearly not attached. On the other hand, if the detector senses the anvil, the carriage moves up (in position control) by a height larger than the height of the anvil's axle (`AnvilHeight`). If during the motion the sensor stops detecting the anvil, it must mean that the anvil is not attached. However, if the motion is completed successfully, it is guaranteed that the anvil is attached. Either way, the variable `AnvilAttached` is set accordingly, and the program moves on.
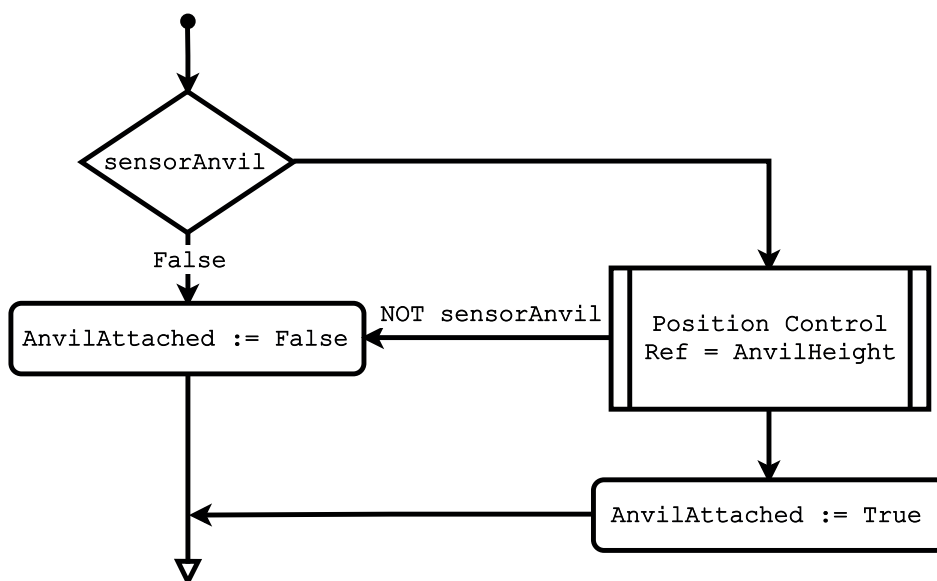

Figure 3.32: `CHECK_ANVIL` subroutine

3.2.5 `Position Control` Subroutine

The `Position Control` subroutine is the subroutine responsible for moving the carriage over a precise distance specified by the variable `Ref`. The exact specifics for the controller implemented are given in chapter 4.

In order to know when the carriage has reached its destined height, the controller has a built-in output that calculates when the carriage is within a very small margin of error of its destined position and has an equally small velocity. The need for both comparisons is that in the case of an overshoot, the error in position at one point will be exactly 0, but since the carriage still has velocity, it will not last. This way, by verifying both velocity and position, it is guaranteed that a steady final position is obtained.

3.2.6 `SOS` Subroutine

When the system senses the inductive detector has been triggered, or when the user triggers an emergency (whether by a signal sent to the computer via the emergency buttons or due to pressing the virtual emergency), the program enters a state of emergency, SOS, shown in fig. 3.33. As mentioned in section 3.1.7, as soon as the electronics sense an emergency state, they will cut power from the actuator (with the exception of the RCS, which will be triggered). When this happens, the program, as a fail-safe, also imitates this by cutting the relevant signals to the actuators.
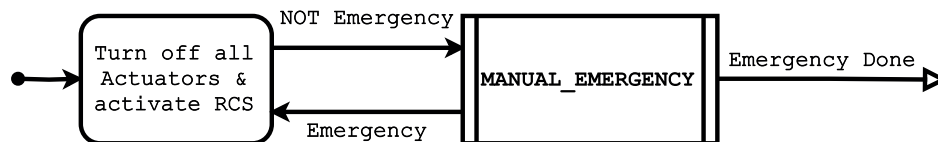
Figure 3.33: SOS subroutine

Once the user is ready to retake control of the machine, it enters into an emergency manual state, MANUAL_EMERGENCY, that has all the same controls present in the MANUAL subroutine, with the addition of the ability to control the velocity acquisition subsystem as well. Once the user is satisfied with the state of the machine, a button can be pressed on the interface to return the machine to regular functioning, starting with the initialization process again.

Chapter 4

Position Control System

Positioning the anvil at a required height is very important for the functioning of a drop-weight test machine since it will be a determining factor in how accurate the tests are. At the maximum weight, 2 mm of error in position roughly corresponds to a 1 J error in the impact energy. This chapter will describe the controller used for moving the motor and the entire tuning process.

4.1 System Modelling

In any control system, before implementing a controller it is necessary to have a good understanding of the behaviour and dynamics of the system being studied. Hence, a mathematical model must be determined.

The system to be modelled in this particular case is the lifting subsystem. It is comprised of the drive, the motor, the gearbox, the pulley and the carriage as depicted in fig. 4.1. When the user inputs a reference height into the interface, the Simulink Stateflow® program handles it and delivers the appropriate variable containing this height to the controller (Ref). The controller then processes this and outputs a reference signal u into the drive, which converts it into the appropriate voltage to drive the motor, v_m. The motor then turns the pulley, which winds and unwinds the cable (depending on direction of motion) and in turn ascends or descends the carriage to position y. The real position of the carriage is inferred from the rotary encoder installed on the motor (see section 3.1.5.2) which counts are represented by the variable N.
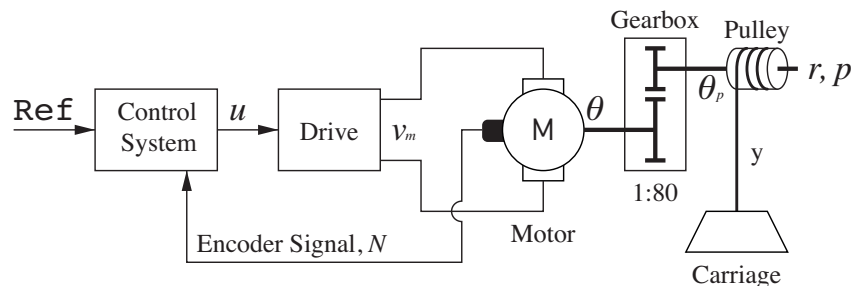

Figure 4.1: Schematic of the lifting system

It is therefore desired to obtain a relation between N and y so that by reading the encoder counts alone, the system knows exactly where the carriage is. From the diagram in fig. 4.1 it is possible to extract the relation between rotation of the motor, θ and change in height of the carriage, y. Let n be the ratio of the gearbox and θ_p be the rotation of the pulley. The equation that models the gearbox and relates θ to θ_p is:

$$\theta_p = \theta \cdot n \tag{4.1}$$

The relation between y and θ is obtained by considering the length of cable unwound from the barrel of the pulley, which has radius r. If the barrel was a simple cylinder, this length would be equal to the arc length of the circle of radius r corresponding to the angle rolled θ. However, as discussed in section 3.1.3, in order to prevent the cable winding up on itself, a helical barrel (with pitch p) was implemented instead of a cylindrical drum. Therefore, the length of cable unwound will be equal to the length L of the helix corresponding to the rotation θ_p of the barrel. To calculate this length, first the length of an entire turn of the helix, L_1 needs to be found.
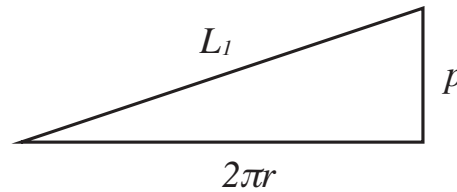

Figure 4.2: Helix of radius r and pitch p unrolled into a flat ramp, showing hypotenuse L_1 equal to the length of the helix

If a helix of radius r and pitch p is unrolled into a flat plane, it forms a ramp similar to the one shown in in fig. 4.2, where the horizontal is the circumference of the circumscribing circle, $2\pi \cdot r$, and the height is the pitch p. Therefore, the length of one turn of the helix can be deduced from:

$$L_1^2 = (2\pi \cdot r)^2 + p^2 \implies L_1 = \sqrt{(2\pi \cdot r)^2 + p^2} \tag{4.2}$$

and therefore, the length L of helix wound by θ_p (in radians) is:

$$L = \frac{\theta_p}{2\pi} \cdot \sqrt{(2\pi \cdot r)^2 + p^2} \tag{4.3}$$

and thus, since the height y of the carriage must be equal to the length of cable wound, the relation between θ_p and y (that models the pulley) becomes:

$$y = \left(\frac{\sqrt{(2\pi \cdot r)^2 + p^2}}{2\pi} \right) \cdot \theta_p \tag{4.4}$$

From equations 4.1 and 4.4 it is then easy to conclude:

$$y = \left(\frac{\sqrt{(2\pi \cdot r)^2 + p^2}}{2\pi} \right) \cdot n \cdot \theta \tag{4.5}$$

As mentioned in section 3.1.5.2, the encoder has an effective resolution of 1200 counts per revolution. It is possible to convert this resolution into a value given in radians, *res*, as follows:

$$res = \frac{2\pi \, \text{rad}}{1200} = 5.23 \times 10^{-3} \, \text{rad} \tag{4.6}$$

This means that for every count of the encoder, the motor shaft has rotated by *res*. Let N be the number of counts from the encoder, angle θ then becomes:

$$\theta = res \cdot N \tag{4.7}$$

And from this and equation 4.5 a relation between encoder counts N and displacement of the carriage y can be found to be:

$$y = \left(\frac{\sqrt{(2\pi \cdot r)^2 + p^2}}{2\pi} \right) \cdot n \cdot res \cdot N \tag{4.8}$$

Constant K_N is then defined and the final equation for the relationship between both variables is found.

$$K_N = \left(\frac{\sqrt{(2\pi \cdot r)^2 + p^2}}{2\pi} \right) \cdot n \cdot res \implies y = K_N \cdot N \tag{4.9}$$

According to the construction drawings done by Ramos, the radius and pitch of the helix are 30 mm and 7 mm respectively, and the ratio of the gearbox is 1:80 [5]. With this, the value of K_N is calculated to be:

$$K_N = 3.93 \times 10^{-3} \, \text{mm per encoder count} \tag{4.10}$$

And thus, the system has been fully mathematically modelled. It is now possible to start designing a PID controller that will control the vertical position of the carriage based on the displacement of the encoder's count signal, which can now be directly translated into the displacement in height of the carriage.

4.2 PID Controller

The PID controller (short for proportional-integral-derivative controller) is by far the most general and ubiquitous type of controller used in industrial control systems. It is a closed-loop feedback system that given a reference control variable, generates a control action as a function of the error that the system has in relation to said reference. As shown in fig. 4.3, the controller has three main

actions based on the error E: Proportional action (K_P), integral action (K_I) and derivative action (K_D). Another way to notate K_I and K_D is to define them in terms of K_P:

$$K_I = K_P/T_I \quad K_D = K_P \cdot T_D \tag{4.11}$$

These signals from these three actions are then added up to generate the final control action u. If K_I or K_D are set to zero, the corresponding action will be nullified. Such controllers are called P, PI, or PD controllers, depending on which action has been removed.

The best way to determine the three constants K_P, T_I and T_D is through direct experimentation and not through calculation, especially if the model is complex [48]. To make the tuning process easier, however, several empirical methods have been created, such as the Shinskey method, the Cohen-Coon method or Ziegler-Nichols' first and second methods, the latter being discussed in section 4.3.1.
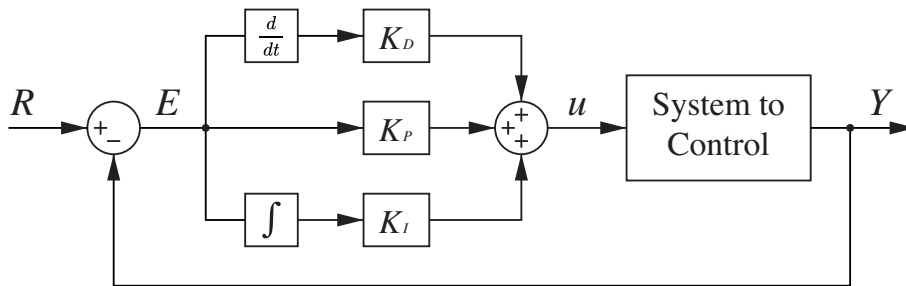

Figure 4.3: General and simplest form of a PID controller

In the case of the lifting subsystem, the PID controller will be controlling the position of the carriage. In fig. 4.4 the Simulink® block diagram responsible for this control is shown. Inlet 2, the encoder signal, already comes converted into the height of the carriage (by multiplying $K_N \cdot N$, as discussed in the previous section).
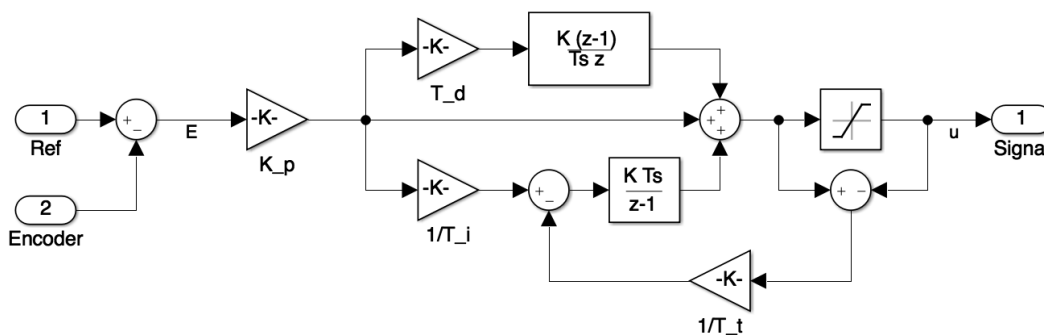

Figure 4.4: Simulink® block diagram of the implemented PID controller

This controller sends its control action u as a voltage value through the DAQ board directly into the drive that controls the motor. However, both the DAQ and the drive cannot send and

receive an arbitrary tension, they are limited to a $\pm10\,$V range. Therefore, the signal coming from the PID controller must be saturated in order to remain in this limited range. This saturation will impair the performance of the controller, and to mitigate this effect, an anti-windup effect must be introduced (also shown in fig. 4.4).

4.3   PID Controller Tuning

The setup for tuning the parameters of the controller was a simple, but rigorous one. Several tests were made for each combination of parameters The carriage was manually placed at the same position (this position was always ensured through the use of the optical and inductive sensors), the encoder signal was reset, and the controller was given a certain reference to arrive at. The tests were repeated for different reference heights in both ascending and descending motion. Presenting all the results in this thesis would prove too extensive, so in order to present results in a comparable way, the tests presented are all in ascending motion to a reference height of 500 mm.

4.3.1   Ziegler-Nichols' Second Method

The method used for tuning the controller was Ziegler-Nichols' second method. This is an experimental method that involves obtaining certain values and using those values to calculate approximate controller parameters to use in its final implementation. Those parameters usually need to be fine-tuned afterwards to ensure the best performance of the controller.

Table 4.1: Ziegler-Nichols' second method parameter calculation

Controller Type	K_P	T_I	T_D
P	$0.5 \cdot K_{cr}$	∞	0
PI	$0.45 \cdot K_{cr}$	$P_{cr}/1.2$	0
PID	$0.6 \cdot K_{cr}$	$0.5 \cdot P_{cr}$	$0.125 \cdot P_{cr}$

The exact methodology of Ziegler-Nichols' second method starts out by using a simple controller exclusively containing proportional action. The proportional parameter K_P^* of this controller is first set to zero and then slowly incremented. For every incrementation of K_P^*, tests are performed recording the step-response of the system to a given reference. K_P^* at first will produce a step-response that will slowly approach the reference from below, and in the limit will have a steady-state error. As it increases, the response will start to overshoot, and eventually will reach a point where it will begin to oscillate in turn of the reference with a constant period. The value of K_P^* for which this happens is denoted K_{cr} for critical proportional constant, and the period of the oscillation is denoted P_{cr}. From these two constants, using table table 4.1, it is possible to calculate the first estimate for the controller parameters.

4.3.2   Ziegler-Nichols' Second Method Results

The tests were first executed by incrementing K_P^* in steps of 500, starting at 500 up to 3000. Since the differences were being quite small, the step size was then increased to 1000. Figure 4.5 shows the first test, performed at $K_P^* = 500$.
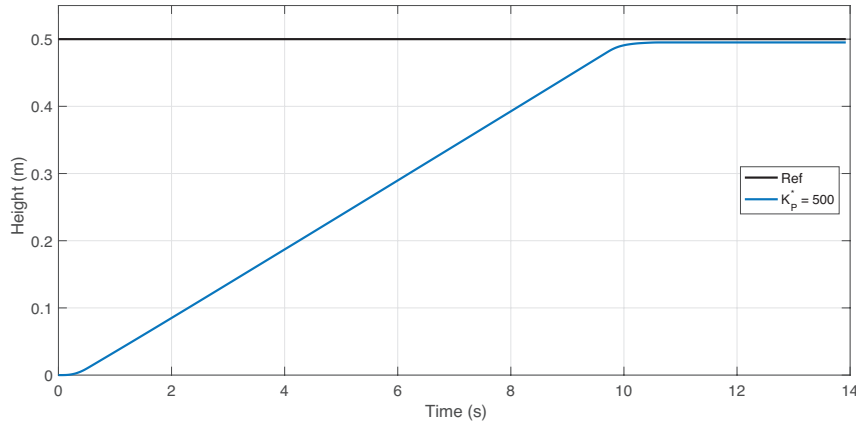

Figure 4.5: First test, $K_P^* = 500$, full view

As expected, the graph approaches the reference but has a steady state error. This first graph shows the full course of the test, from time $0\,\text{s}$ onwards. The behaviour of the tests for the first few seconds of the test, however, is always the same, having the same ramp, so from then on, all graphs only include the last part of the test, when they come close to the reference, This is where their behaviour diverges, and where the Ziegler-Nichols method can be applied. The behaviour shown in fig. 4.5 can be seen better in fig. 4.6 as well as the behaviours of subsequent tests.
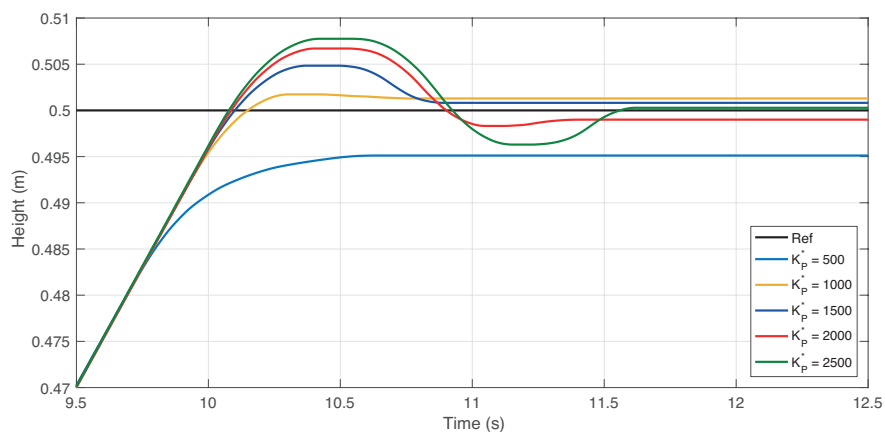

Figure 4.6: $K_P^* = 500$ to 2500

The effect of increasing K_P^* can be clearly seen in this figure. Not only is the error in position becoming smaller and smaller, the oscillatory behaviour is increasing. It is expected for a

proportional controller that the steady-state error e_{ss} approximately follow the rule [49]:

$$e_{ss} = \lim_{t \to \infty} E(t) = \frac{1}{1 + K_P} \tag{4.12}$$

Therefore, the largest the value of K_P^*, the smaller the error. However, a larger K_P^* will also introduce more instability, and will even reach a limit cycle oscillatory behaviour, which is almost always unwanted.
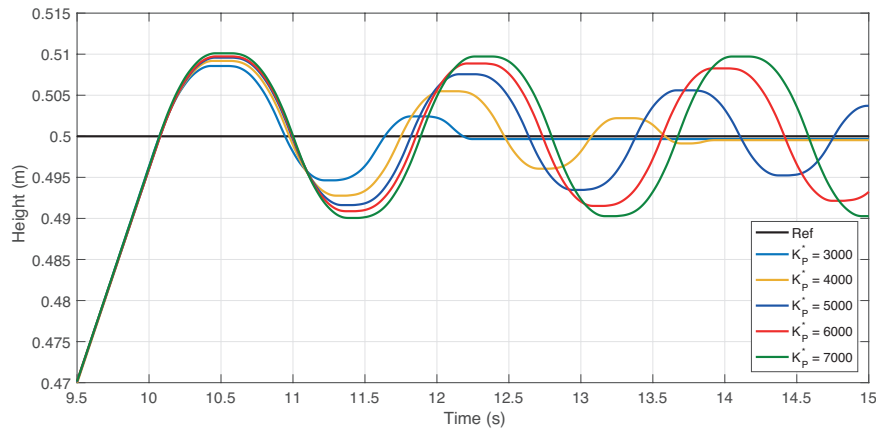

Figure 4.7: $K_P^* = 3000$ to 7000

Figure 4.7 shows the rest of the tests performed, in steps of 1000 each. The behaviour of increasing K_P^* is now even more apparent, and with $K_P^* = 7000$, it finally reaches a limit cycle. Figure 4.8 shows this last test isolated for better reference.
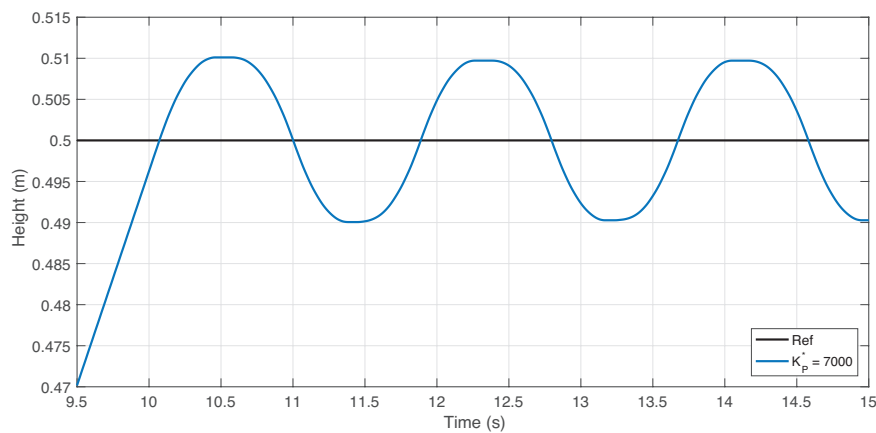

Figure 4.8: $K_P^* = 7000$

Therefore, the critical proportional constant K_{cr} is concluded to be 7000. A few more tests were run, and the critical period P_{cr} was taken from each, and an average was calculated. The final

value of P_{cr} was found to be 1.83 s. From this, using table 4.1 it is possible to obtain values for and to implement the parameters of the controllers to test.

There are three controllers that can be tested: a proportional controller (P), a PI and a PID. Since the range of K_P tested covered the recommended value for K_P given by table 4.1, 4500, it is safe to ignore it, since it will have an oscillatory behaviour with a very long settling time, which is highly unwanted. Therefore, only the PI and PID controller were tested. The values given by Ziegler-Nichols' Second method are:

$$\text{PI:} \quad K_P = 3150\,\text{V/mm} \quad T_I = 1.525\,\text{s} \quad T_D = 0\,\text{s}$$
$$\text{PID:} \quad K_P = 4500\,\text{V/mm} \quad T_I = 0.915\,\text{s} \quad T_D = 0.228\,75\,\text{s} \tag{4.13}$$

Figure 4.9 shows the results of one of those tests only, since the results of both tests were indistinguishable.
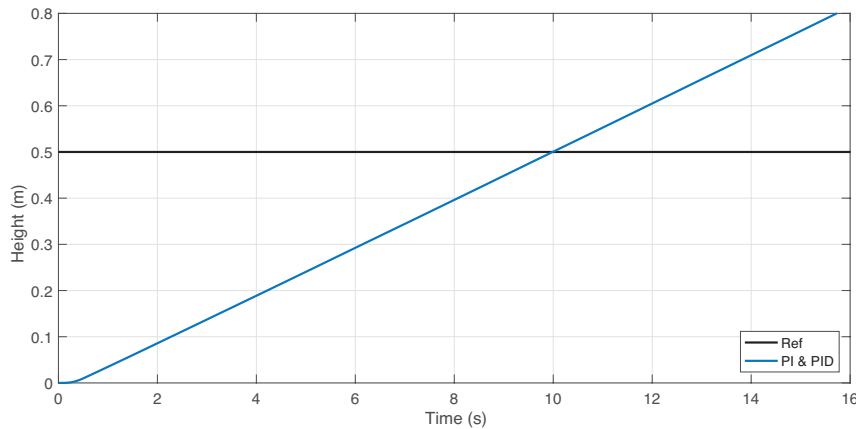

Figure 4.9: PI and PID controller test, only one graph shown since result was the same

As can be clearly seen, the controllers do not work at all. The carriage shoots way past the reference and does not exhibit any signs that it is slowing down. The tests always had to be stopped by hand in order to prevent the carriage from triggering the inductive sensor at the top of the machine. This behaviour could either be due to the Ziegler-Nichols method failing or due to the fact that the anti-windup is missing. Analysing the control action u of these controllers before saturation, depicted in fig. 4.10, shows that it's the latter option.

The control action, throughout the entire course of the test, is orders of magnitude larger than the saturation point (10 V) and so, is permanently saturated. Therefore, an anti-windup effect needs to be implemented. It was decided to discard the PI controller and only maintain the PID for this process.

The anti-windup effect can be seen implemented in fig. 4.11. In order to resolve the saturation problem, the system needs to somehow be aware of the effect of the saturation. Furthermore, due to the saturation, the integral action will easily grow very large (windup), and hence, this is the critical action to reduce. By getting the difference between the saturated and non-saturated
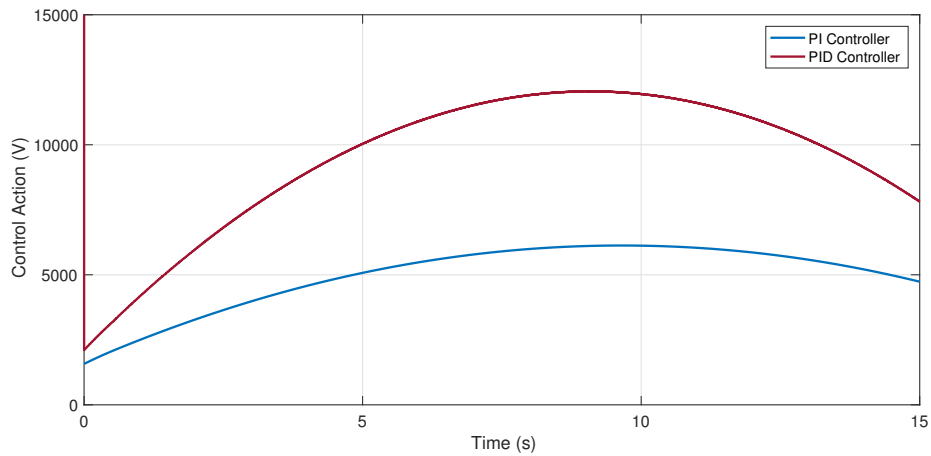
Figure 4.10: Control action u of PI and PID controllers

signals, dividing it by a time constant and subtracting it from the integral action, this windup effect is greatly reduced.
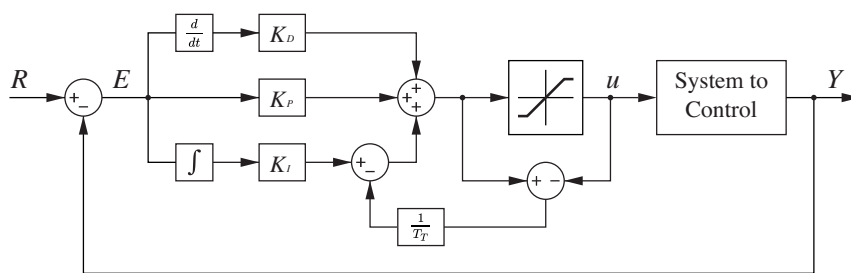

Figure 4.11: General PID controller with anti-windup

In order implement the anti-windup, the time constant T_T must be introduced. Much like with the Ziegler-Nichols method, this is an empirical value, but there are ways of approximating it. One of the guidelines for choosing an appropriate T_T is to have $T_D < T_T < T_I$ [50], and so, one of the ways that are generally used is to take the geometric mean of both T_I and T_D [51], in other words:

$$T_T = \sqrt{T_I \cdot T_D} = 0.4575\,\text{s} \tag{4.14}$$

Implementing this into the PID controller produced the following results, shown in fig. 4.12.
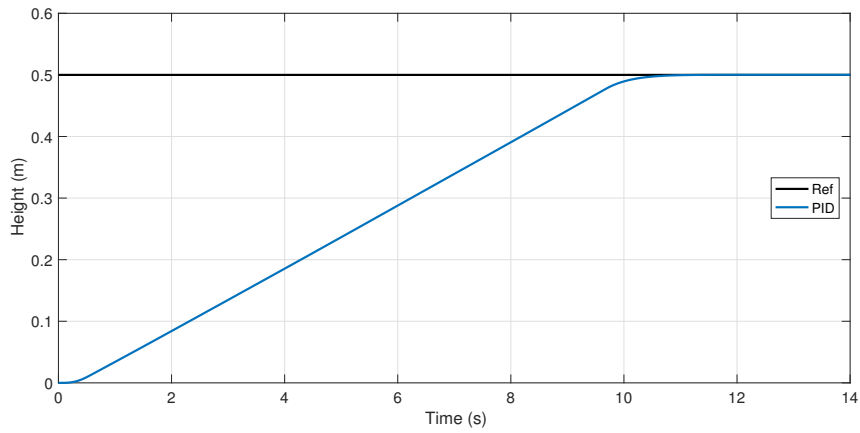
Figure 4.12: PID controller with anti-windup

The new controller with anti-wind up no longer exhibits problems due to saturation, has a very fast settling time and null steady-state error, as can be seen by the close-up on fig. 4.13.
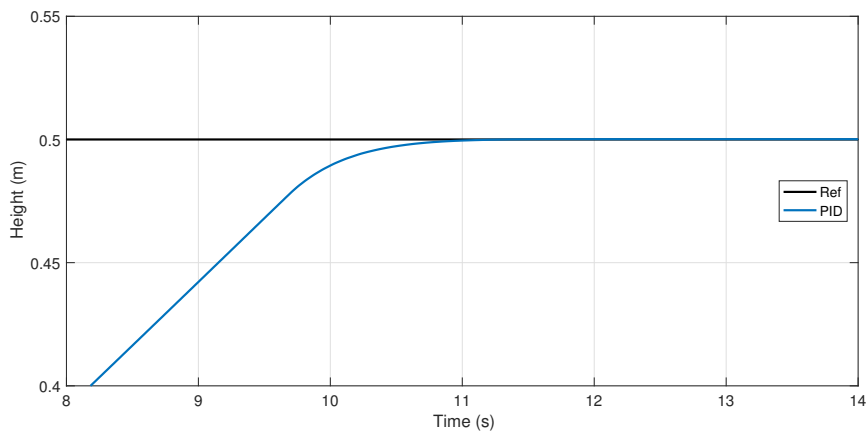

Figure 4.13: Close-up of fig. 4.12

The PID controller was also tested with various weights: just the carriage, carriage with anvil and carriage with anvil and a 5 kg weight. The results are shown in fig. 4.14
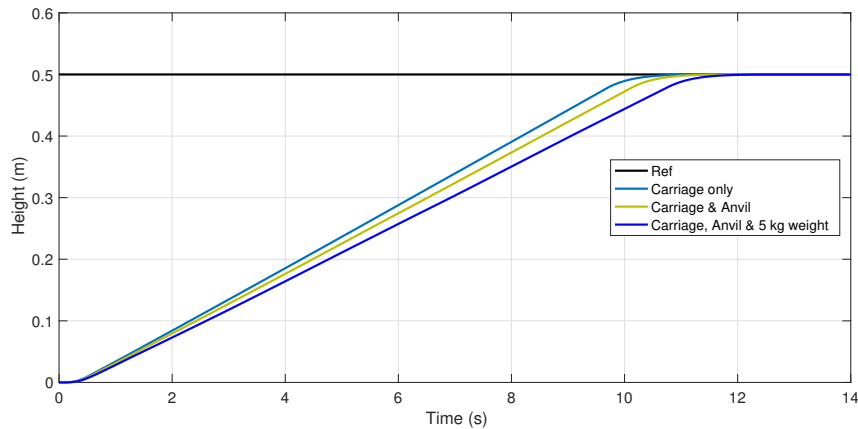
Figure 4.14: PID controller with various tests

4.4   Measurement Error Correction

During the tests performed on the controller, an anomaly was noticed in the way the system was interpreting dimensions. While the PID controller was being well positioned in relation to the reference signal in a very repeatable fashion, the reference signal did not correspond to a real life distance. There seemed to be a constant and proportional error between the distance the computer thought it moved and the distance actually moved by the carriage. In other words, if the carriage was ordered to move up and then down by the same distance, it would return to the exact starting point, but it would've moved a larger distance than the one requested.

Figure 4.15: LVDT setup

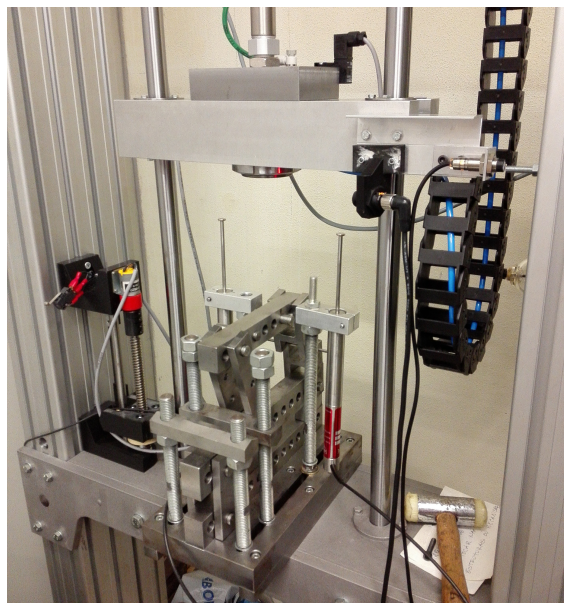In order to solve this problem, an experiment was designed using a pair of linear variable differential transformers (LVDTs). ADFEUP owns some high-resolution LVDTs that are significantly more precise than the encoder on the motor. By placing them under the carriage and slowly lowering it, it was possible to record the position of the carriage with the encoder and the LVDTs simultaneously, and it was possible to compare both results. The experimental setup is shown in fig. 4.15 and the carriage pressing down on the LVDTs is shown in fig. 4.16.
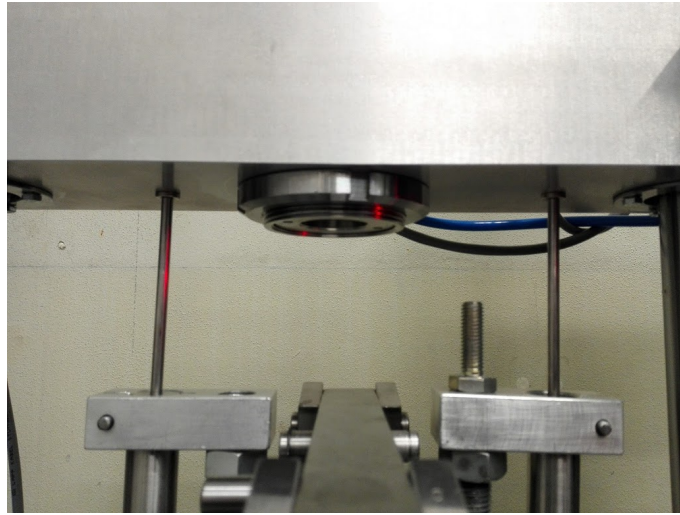

Figure 4.16: Carriage lowering onto LVDTs

The LVDTs when used produce a voltage signal as a function of the distance along its stroke (which is captured by data acquisition equipment). The characteristic curve of an LVDT has two non-linear zones at both extremes of its stroke, and a linear portion in the centre. Care was taken to perform the test exclusively in the linear zone. The linear zones of both LVDTs used had been previously calibrated individually for other uses, and their equations that relate output voltage V to distance s are:

$$\begin{matrix} \text{LVDT 1:} & V_1 = 5.1446 \cdot s + 25.499 \\ \text{LVDT 2:} & V_2 = 5.1367 \cdot s + 25.674 \end{matrix}, \quad R^2 = 0.99999 \qquad (4.15)$$

After obtaining the values for distance recorded by the LVDTs, the absolute displacement was calculated for each individual LVDT (by subtracting the initial distance recorded) and the average of both displacements was calculated. The results, as compared to the encoder signal are present in fig. 4.17.

At the end of the experiment, the displacement recorded by the LVDTs was 38.99 mm while the encoder recorded 39.75 mm which is approximately a 2% error. From this, a correction factor ε was calculated:

$$\varepsilon = 1 - \frac{|38.99 - 39.75|}{38.99} = 0.9808364 \qquad (4.16)$$
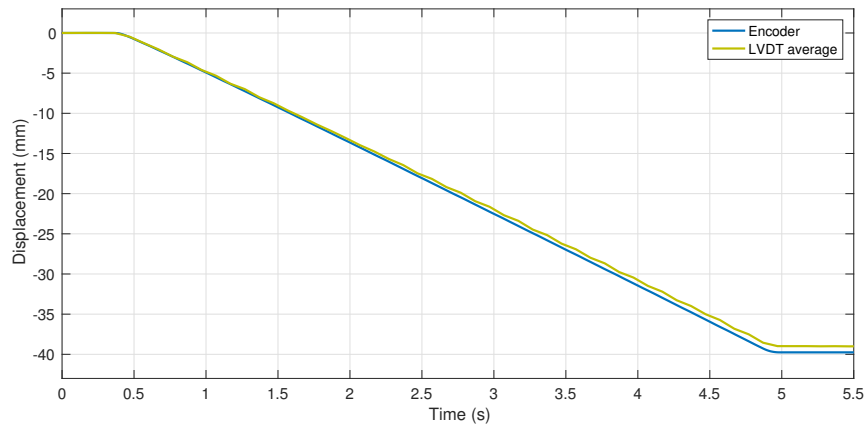
Figure 4.17: Experiment results

In the model, this number was applied as a gain right at the entry of the encoder signal, which made the computer interpret the encoder signal correctly.

Having finished the error correction stage, the position control was finished. Therefore, the entirety of the software and hardware for the machine was completed, starting with the electronics design and assembly, the command sequence design and implementation, and the control system for the lifting motor. Thus, the framework for the machine was finalized.

Chapter 5

Conclusion

As stated in section 1.4, the main objectives of this thesis were the design of the rebound-capture system, the design and assembly of the electrical system and the implementation of the command and control software for ADFEUP's drop-weight test machine, for testing adhesives and adhesive joints.

The design of the RCS has been successfully completed and simulations have been performed that validate and guarantee its good functioning under the conditions required for the drop-weight test machine. The system is ready to enter production and implementation on the machine structure.

The electronics cabinet has not only been designed but also fully implemented, tested and utilised. Everything from the power supply, to the detectors, to the signal acquisition system has proven to work exactly as intended. The circuit diagrams have also been completely finished in order to keep a record of how everything works and is assembled. In the eventuality that the circuit ever needs to be altered or built upon, all measures have been taken to make that process as simple as possible.

Similarly, the command software has not only been designed, but the fully functional Simulink® program has been created and thoroughly tested. The command sequence suffered many changes from the one proposed by Ramos [5] to make the program's structure as easy as possible to work with.

Every functionality of the program has been coded and can be used, albeit the current lack of a user interface makes the program very difficult to use. But in the future, once a graphical user interface is implemented, using the machine will be made very user-friendly thanks to the new command sequence implemented.

The velocity acquisition system can already deliver results, so once an accelerometer is installed to obtain information about the impact, the machine will be fully instrumented and as far as automation is concerned, it will be ready for testing. Finally, the control system for the lifting motor was designed and implemented and its accuracy was corrected in order to guarantee that the tests performed once the machine is ready are as accurate as possible.

Each one of these objectives has been successfully completed, and the machine, though unfinished, is currently very close to being able to perform fully instrumented tests.
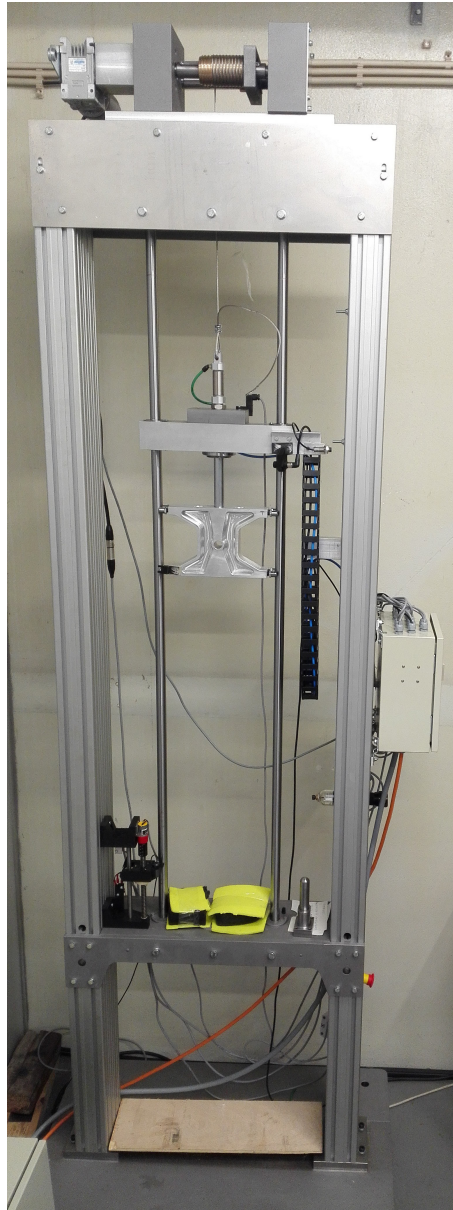

Figure 5.1: Assembled machine

5.1 Future Work

As mentioned, building the drop-weight test machine is a large project that has involved many people and has been the focus of four different theses including this one. The machine is very close to being completed and fully-functional, but there is still much work that needs to be done in order to finalise it.

First of all, the most important part of the machine that is currently missing is the accelerometer. This component was suggested to be implemented by Ramos [5] and will be responsible for acquiring crucial data regarding the forces at work during the impact. Therefore, installing it is of highest priority.

Many of the mechanical subsystems of the machine have been installed, but in order for the machine to function at its full potential, they still need to be tuned (for example the anvil needs to be very carefully placed in the guiding rails). There also needs to be an evaluation of the masses of the several components of the anvil, including the body of the anvil itself, the impactor, the accelerometer, the weight supports and weights (the latter three still to be installed) to guarantee full knowledge of how much mass is being used for each test.

Since the rebound-capture system has been designed, its installation is also very important, not only because it is necessary for the tests themselves, but also because it acts as an emergency safeguard, so performing tests without it is a safety hazard.

On the same line of thought, a more robust safety system needs to be designed for the machine, consisting of some sort of barrier between the user and the inside of the structure during tests. Without such a barrier, there is a serious risk of injury through projectile expulsion from the test samples as well as the obvious danger present from having no barrier between the user and a falling 56 kg weight. Any sensors present in this security system also need to be coded into the command sequence and Simulink Stateflow® logic.

Finally, a graphical user interface needs to be designed and implemented alongside the already made Simulink® program in order to make it as easy to use as possible.
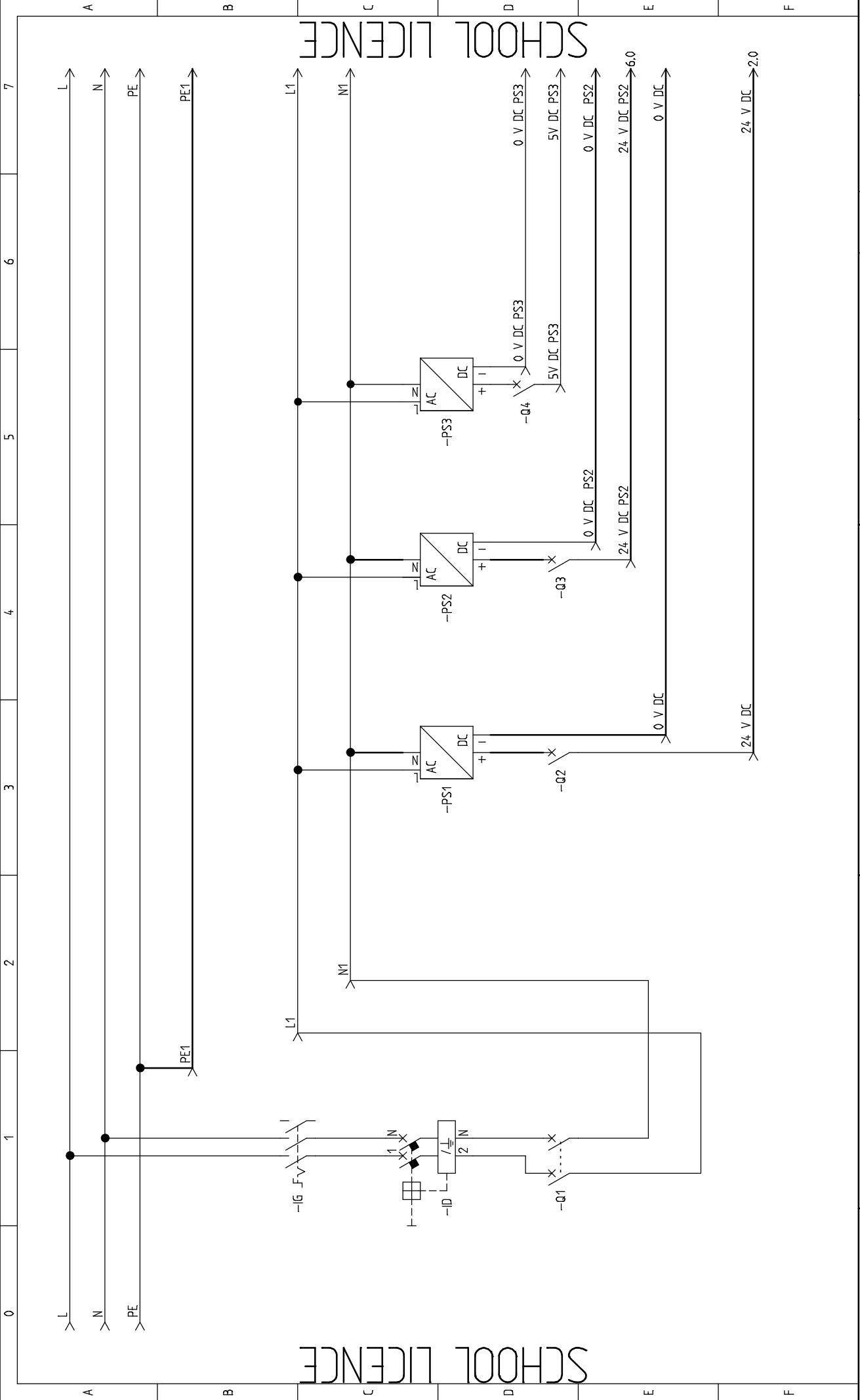
References

[1] Lucas Filipe Martins da Silva, António Goncalves de Magalhães, and Marcelo Francisco SF de Moura. *Juntas Adesivas Estruturais*. Publindústria, 2007.

[2] JJM Machado, EAS Marques, and Lucas FM da Silva. Adhesives and adhesive joints under impact loadings: An overview. *The Journal of Adhesion*, pages 1–32, 2017.

[3] ASTM ASTM D950-03(2011). Standard test method for impact strength of adhesive bonds. Technical report, ASTM, 2011.

[4] Instron. *CEAST 9300 Series*, 4 2011.

[5] André Filipe Lemos Antunes Palma Ramos. Development of a machine to measure the impact strength of adhesive joints. 2016.

[6] Zwick Roell. *Drop Weight Tester HIT230F for tests on plastics*.

[7] Zwick Roell. *Drop Weight Tester HIT230F - Pre-damage of plates made of composites for CAI tests*.

[8] Zwick Roell. *High Energy Drop Weight Testers DWT60 / DWT80 / DWT100*.

[9] Imatek. *IM10 Type R Drop Weight Impact Testers*.

[10] Imatek. *IM10T Drop Weight Impact Testers*.

[11] Carlos Manuel Castillo de Castro. Desenvolvimento de um dispositivo experimental para medir a resistência ao impacto de ligações adesivas. 2014.

[12] Rui Manuel Couto Barbosa. Conceção e automatização de um dispositivo para medir a resistência ao impacto de ligações adesivas. 2014.

[13] Festo. *Round cylinders DSNU/DSNUP/DSN/ESNU/ESN*, 6 2017.

[14] Festo. *Solenoid valves MH2/MH3/MH4, fast-switching valves*, 7 2016.

[15] Festo. *Mounting components*, 3 2017.

[16] Festo. *Piston rod attachments*, 3 2017.

[17] ACE. *Safety Shock Absorbers SCS33 to SCS64*, 6 2011.

[18] ACE. *Industrial Shock Absorbers MC33*, 8 2010.

[19] INA. *Needle roller bearings NA4907-2RSR-XL (Series NA49..-2RSR*, 6 2017.

[20] INA. *Thrust washers EGW42-E40-B (Series EGW..-E40-B)*, 6 2017.

[21] ISO. Pneumatic fluid power — determination of flow-rate characteristics of components using compressible fluids. Technical report, ISO, 1989.

[22] Bruce Roy Munson, Donald F Young, and Theodore H Okiishi. Fundamentals of fluid mechanics. *New York*, 3(4), 1990.

[23] J Falcão Carneiro and F Gomes de Almeida. Reduced-order thermodynamic models for servo-pneumatic actuator chambers. *Proceedings of the Institution of Mechanical Engineers, Part I: Journal of Systems and Control Engineering*, 220(4):301–314, 2006.

[24] C Canudas De Wit, Hans Olsson, Karl Johan Astrom, and Pablo Lischinsky. A new model for control of systems with friction. *IEEE Transactions on automatic control*, 40(3):419–425, 1995.

[25] Karl Johanastrom and Carlos Canudas-de Wit. Revisiting the lugre friction model. *IEEE control Systems*, 28(6):101–114, 2008.

[26] YANG Junhong, Andrew Plummer, and XUE Yong. Dynamic friction modelling without drift and its application in the simulation of a valve controlled hydraulic cylinder system. *Journal of Advanced Mechanical Design, Systems, and Manufacturing*, 8(6):JAMDSM0075–JAMDSM0075, 2014.

[27] Paulo Pereira. Modelação da força de atrito de um servomecanismo pneumático utilizando o modelo de lugre. 2013.

[28] MatWeb. Aisi 1045 steel, cold drawn, 19-32 mm (0.75-1.25 in) round, 2017.

[29] MatWeb. Alclad aluminum 6061-t6, t651, 2017.

[30] MFA/Como Drills. *918D SERIES 25mm SINGLE RATIO METAL GEARBOX*.

[31] ST. *L298 - Dual Full-Bridge Driver*, 1 2000.

[32] RS. *Inductive Sensor*.

[33] OMRON. *Photoelectric Sensors E3FA/E3RA/E3FB/E3RB*, 2012.

[34] OMRON. *Slot-type Photomicrosensor (Non-modulated) EE-SX47/67*, 4 2011.

[35] Cherry. *D4 miniature switch*.

[36] Transtecno. *Motoriduttori CC a vite senza fine / DC wormgearmotors*.

[37] Electromen. *EM-12A PWM DC-MOTOR CONTROL UNIT 24V 8A 200W*.

[38] SMC. *ISO Cylinder Series C85*.

[39] Parker. *B Series Valves*, 12 2006.

[40] Parker. *B Series High Performance Industrial Valves*.

[41] Measurement Computing. *PCIM-DDA06/16 Analog Output and Digital I/O Board User's Guide*, 2012.

[42] Intecno. *ME22 MICRO Encoder*, 2015.

[43] Measurement Computing. *PCI-QUAD04 - Quadrature Encoder Input - User's Guide*, 6 2016.

[44] CEL. *Photocoupler PS2502-1,-4,PS2502L-1,-4*, 9 2009.

[45] RS Pro. *RS Pro 240W Single Output Industrial DIN Rail Power Supply DRP-240 Series*, 6 2014.

[46] RS Pro. *RS Pro 96W Single Output Industrial DIN Rail Power Supply MDR-100 Series*, 10 2015.

[47] RS Pro. *RS Pro 10W Single Output Industrial DIN Rail Power Supply MDR-10 Series*, 11 2011.

[48] Katsuhiko Ogata and Yanjuan Yang. *Modern control engineering*. Prentice-Hall Englewood Cliffs, NJ, 1970.

[49] J Tenreiro Machado, António M Lopes, Alexandra M Galhano, and Duarte Valério. *Solved Problems in Dynamical Systems and Control*. The Institution of Engineering and Technology (IET), Stevenage, UK, 2016.

[50] Karl Johan Astrom and Lars Rundqwist. Integrator windup and how to avoid it. In *American Control Conference, 1989*, pages 1693–1698. IEEE, 1989.

[51] Karl Johan Aström and Richard M Murray. *Feedback systems: an introduction for scientists and engineers*. Princeton university press, 2010.
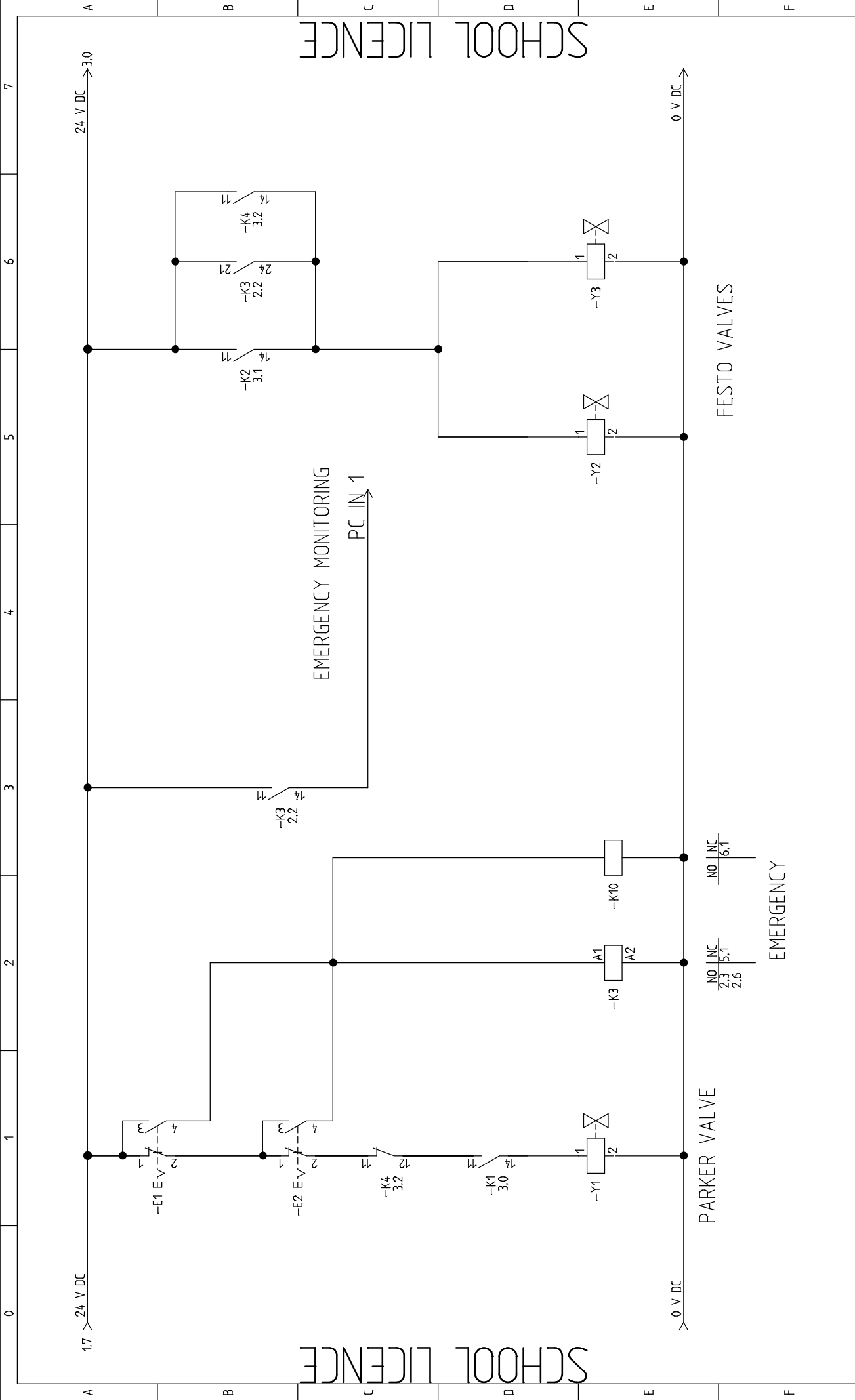
Appendix A

Electric Circuit Diagrams

Project: DWM Circuits	Drawing no.:	Sheet: 1
Date: 12-11-2016	Function:	Location:	Init.:	Rev.:	Next sheet: 2
		Total sheets: 10

— Logo —

24 V DC →3.0

0 V DC →

EMERGENCY MONITORING

PC IN 1

-K3
2.2

-K2
3.1

-K4
3.2

-K3
2.2

-K10
NO | NC
6.1

-K3
2.3
2.6
NO | NC
5.1
A1
A2

EMERGENCY

-Y3

-Y2

FESTO VALVES

PARKER VALVE

-E1 Ev

-E2 Ev

-K4
3.2

-K1
3.0

-Y1

1.7 → 24 V DC
→3.0

0 V DC →

— Logo —

PS2502-4

DAQ Board

0 V DC

24 V DC

0 V PC

PortB1
PortB2
PortB3
PortB4
PortB5

390
390
390
390
390
390
390
390
390

PC OUT 5
PC OUT 4
PC OUT 3
PC OUT 2
PC OUT 1

-9
-8
-7
-6
-5

-K9 A1 A2
-K7 A1 A2
-K4 A1 A2
-K2 A1 A2
-K1 A1 A2

NO NC 6.2
NO NC 4.1
NO NC 2.6 5.1 6.1
NO NC 2.6
NO NC 2.1

Project:	Drawing no.:		Init.:	Rev.:	Sheet:
DWM Circuits					3
Date:	Function:	Location:	Total sheets:		Next sheet:
15-11-2016			10		4

PC OUT

= Logo =

SCHOOL LICENCE

24 V DC → 5.0

3.7 > 24 V DC → 5.0

0 V DC →

0 V DC →

5V DC PS3

PortB0

PortB6

PortB7

D GND

+ 5V

−36

−10

−11

−4

−3

−K5
5.1

−K6
5.3

−K7
3.2

OUT2

OUT1

IN2

IN1

EN A

+ 5V

GND

+12

L298N

−M

Project:	Drawing no.:		Rev.:	Sheet:
DWIM Circuits		Init.:		4
Date:	Function:	Location:	Total sheets:	Next sheet:
27−11−2016			10	5

Velocity Acquisition Motor

— Logo —

— Logo —

Project: DWIM Circuits	Drawing no.:	Init.:	Rev.: 5
Date: 27-11-2016	Function:	Location:	Sheet:
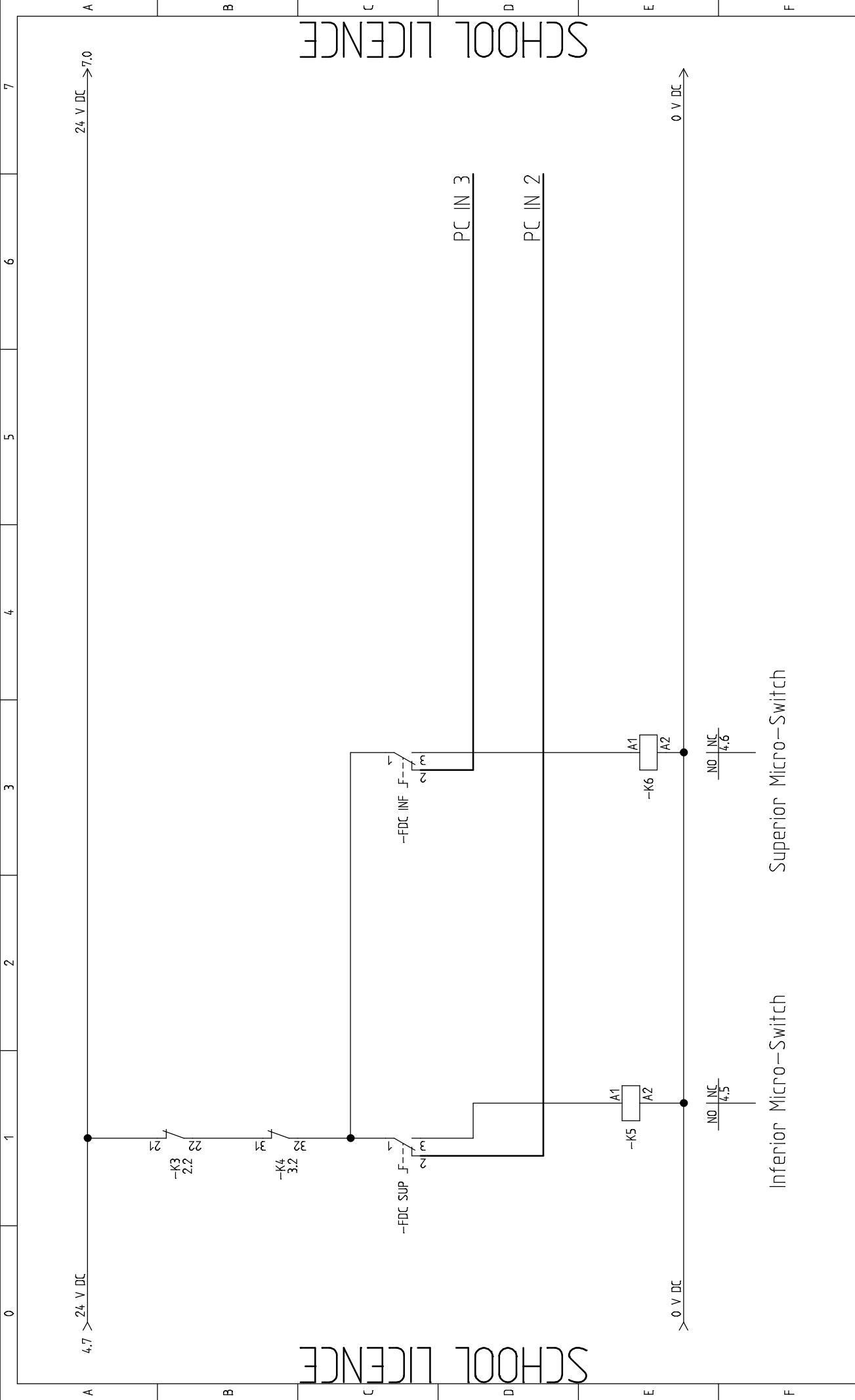
Micro-Switches

Superior Micro-Switch

Inferior Micro-Switch

24 V DC →7.0

0 V DC →

PC IN 3

PC IN 2

-FDC INF

-K6 A1 A2

NO NC 4,6

-FDC SUP

-K5 A1 A2

NO NC 4,5

-K3 2,2 21 22

-K4 3,2 31 32

4,7 > 24 V DC

0 V DC →

Total sheets: 10

Next sheet: 6

MOTOR DRIVE DETAIL

24 V DC PS2

0 V DC PS2

LL GND

0 V −19

9

8

7

6

5

4

3

2

1

V 0l − / + −18

AOUT0

−M

MOTOR DRIVE

−K10
2.3
11
12

−K4
3.2
21
22

−K8
8.4
11
12

−K9
3.3
11
14

1

2

−C1
2200 uF

24 V DC PS2
1.7

0 V DC PS2

SCHOOL LICENCE

SCHOOL LICENCE

24 V DC → 8.0

PCIN6

−K11
7.4

0 V DC

24 V DC
5.7

0 V DC

BROWN

BLACK

BLUE

PINK

A1
A2
−K11

NO | NC
7.5

OMRON E3FA-DN23

Logo

Inductive Detector Monitoring   PC IN 5

24 V DC
9.0

7.7 > 24 V DC

0 V DC

0 V DC

BROWN

BLACK

BLUE

-K8

NO | NC
6.1

Logo

IME12-04PS ZW K F38

Project: DWM Circuits	Drawing no.:		Init.:	Rev.:	Sheet: 8
Date: 28-11-2016	Function:	Location:		Total sheets: 10	Next sheet: 9
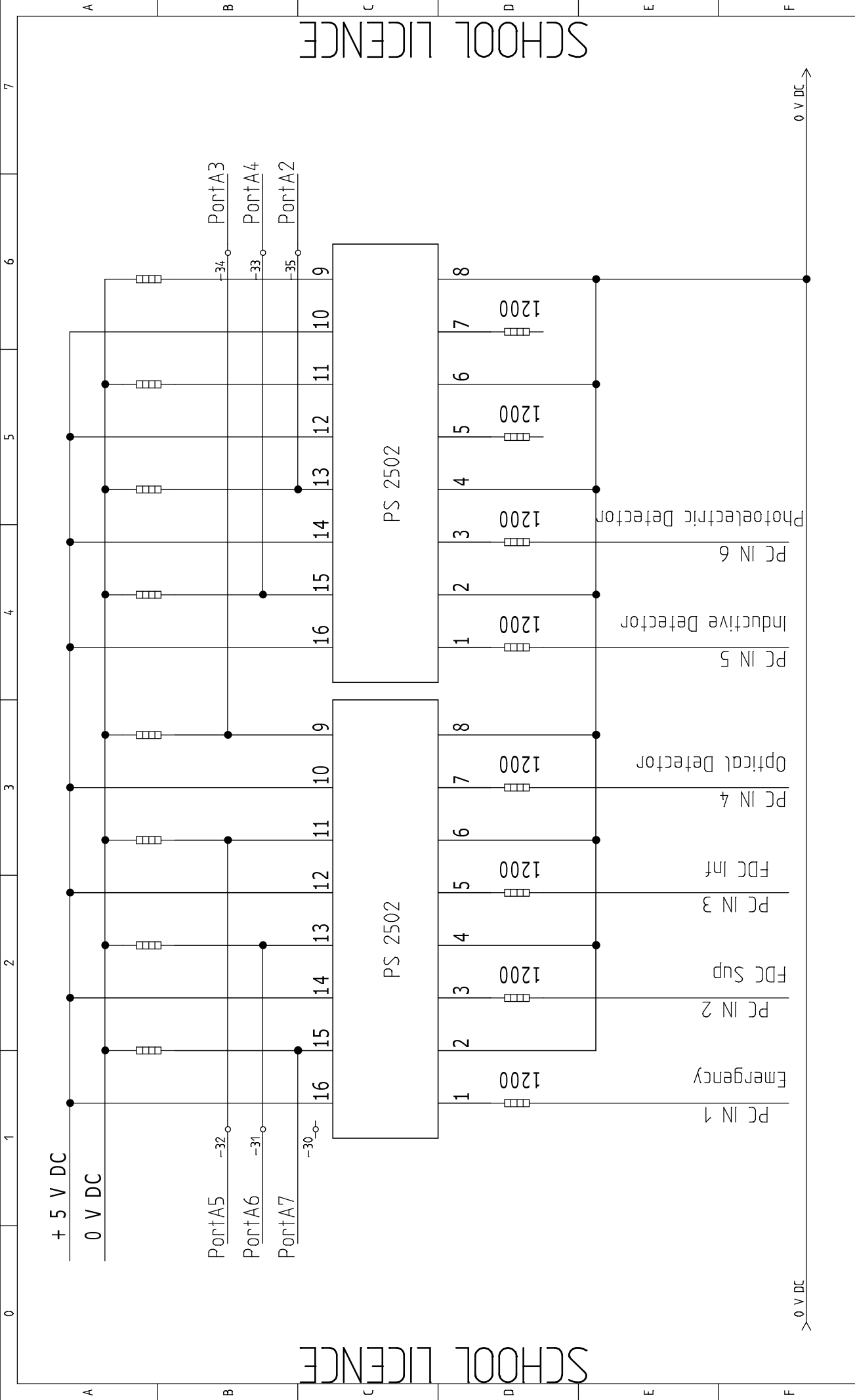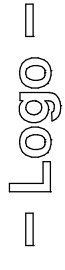
SCHOOL LICENCE

SCHOOL LICENCE

24 V DC

8.7 > 24 V DC

0 V DC

0 V DC

PCIN4

-K12
9.4

14
11

A1
A2

-K12

NO NC
9.5

BROWN

BLACK

BLUE

PINK

OMRON EE-SX670-WR 1M

Project: DWM Circuits
Date: 28-11-2016

Sheet: 9
Next sheet: 10
Total sheets: 10

Logo

+ 5 V DC
0 V DC

PortA5 −32
PortA6 −31
PortA7 −30

PortA3 −34
PortA4 −33
PortA2 −35

PS 2502
PS 2502

0 V DC
0 V DC

1200

PC IN 1
Emergency
PC IN 2
FDC Sup
PC IN 3
FDC Inf
PC IN 4
Optical Detector

PC IN 5
Inductive Detector
PC IN 6
Photoelectric Detector

9 10 11 12 13 14 15 16
8 7 6 5 4 3 2 1

Project: DWM Circuits
Date: 01-12-2016
Drawing no.:
Function:
Init.:
Location:
Rev.:
Sheet: 10
Total sheets: 10
Next sheet:

PC IN

Appendix B

Simulink Stateflow® Program Variables

Table B.1: Simulink Stateflow® program variables and their descriptions

Variable	Initial Value	Type	Description
EncoderPos	-	Input	Current encoder position in counts
manualVel	-	Input	Velocity for manual control set by user
CalcHeight	-	Input	Test height
AtPos	-	Input	Carriage has arrived at set position
Emergency	-	Input	Emergency flag
emergencyDone	-	Input	End emergency mode instruction
manualVel_Em	-	Input	Velocity for manual control in emergency mode set by user
motorUp_Em	-	Input	Emergency mode instruction to raise motor
motorDown_Em	-	Input	Emergency mode instruction to lower motor
manualRelease_Em	-	Input	Release anvil instruction in emergency mode
manualVELAQ_Down_Em	-	Input	Emergency mode instruction to lower velocity acquisition motor
manualVELAQ_Up_Em	-	Input	Emergency mode instruction to raise velocity acquisition motor
beginManual	-	Input	Begin manual mode instruction
manualDone	-	Input	End manual mode instruction
manualRelease	-	Input	Release anvil instruction in manual mode
beginTest	-	Input	Begin test mode instruction
cancelTest	-	Input	Instruction to stop test mode
testLift	-	Input	Instruction to begin lifting carriage to test height
testRelease	-	Input	Release anvil instruction in test mode
motorDown	-	Input	Manual mode instruction to lower motor
motorUp	-	Input	Manual mode instruction to raise motor
sensorInd	-	Input	Signal from inductive sensor
sensorAnvil	-	Input	Signal from photoelectric detector
sensorZero	-	Input	Signal from optical sensor
currTime	-	Input	Current time
FDC_Inf	-	Input	Signal from lower micro-switch
FDC_Sup	-	Input	Signal from upper micro-switch
VELAQ_DOWN	0	Output	Velocity acquisition motor decending motion
VELAQ_UP	0	Output	Velocity acquisition motor ascending motion
VELAQ_Enable	1	Output	L298N board ENAport
VELAQ_Power	1	Output	Power for velocity acquisition motor
PosControl	0	Output	Initialise position control
Ref	0	Output	Position reference for anvil
motorVel	0	Output	Motor velocity for velocity control
AnvilRelease	0	Output	Anvil release order
InductiveOverride	0	Output	Inductive detector override
realVel	-1	Output	Real impact velocity
AnvilAttached	0	Local	Status of anvil attachment
t0	0	Local	Internal variable for calculating realVel
t1	0	Local	Internal variable for calculating realVel
AnvilHeight	0.18	Const	Height of the anvil axel
VELAQ_Dist	0.015	Const	Distance between prongs of the anvil velocity acquisition comb